On the Vertical Structure of Oceanic Mesoscale Tracer Diffusivities

Wenda Zhang and Christopher L. P. Wolfe

School of Marine and Atmospheric Sciences, Stony Brook University, Stony Brook, NY, USA

Key Points:

- The vertical structure of the isopycnal tracer diffusivity is diagnosed by a multiple tracer inversion method in an idealized model.
- The upper-ocean mixing is well represented by the root mean squared eddy velocity times a depth-independent energy-containing scale.
- The deep-ocean mixing follows the vertical structure of the eddy kinetic energy and is attributed to the decay of linear waves.

Corresponding author: Wenda Zhang, wenda.zhang@stonybrook.edu

Abstract

Isopycnal mixing of tracers is important for ocean dynamics and biogeochemistry. Previous studies have primarily focused on the horizontal structure of mixing, but what controls the vertical structure is still unclear. This study investigates the vertical structure of the isopycnal tracer diffusivity diagnosed by a multiple-tracer inversion method in an idealized basin circulation model. The first two eigenvalues of the symmetric part of the 3D diffusivity tensor are approximately tangent to isopycnal surfaces. The isopycnal mixing is anisotropic, with principle directions of the large and small diffusivities generally oriented along and across the mean flow direction. The cross-stream diffusivity can be reconstructed from the along-stream diffusivity after accounting for suppression of mixing by the mean flow. In the circumpolar channel and above the thermocline in the gyres, the vertical structure of the along-stream diffusivity follows that of the rms eddy velocity, with the depth-independent constant of proportionality a local energy-containing scale defined by the peak of the surface eddy kinetic energy (EKE) spectrum. The diffusivity below the thermocline in the gyres instead follows the profile of the EKE times a depth-independent mixing time scale. The transition between the two mixing regimes is attributed to the dominance of nonlinear interactions and linear waves in the upper and deep ocean, respectively. A scaling is proposed that accounts for both regimes and captures the vertical variation of diffusivities better than extant theories. These results inform efforts to parameterize the vertical structure of isopycnal mixing in coarse-resolution ocean models.

Plain Language Summary

Ocean mesoscale eddies mix momentum, heat, carbon and other tracers, which impacts the ocean environment and Earth's climate. The mixing of tracers by mesoscale eddies was mostly measured on the surface, but the observation of the mixing in the ocean interior is rare. It is unclear how eddy mixing varies with depth. We estimated the mixing by mesoscale eddies in an idealized numerical model, which simulates ocean currents and eddies in a basin like the Atlantic Ocean. Mixing decreases with depth in the same rate as the characteristic swirling velocity of eddies in the upper ocean, while it decreases faster in the deep ocean. This is because as eddies become weak in the deep ocean they behave like waves rather than closed swirls. A method accounting for this vertical variation is proposed which recovers the vertical structure of eddy mixing over full depth, once the characteristic swirling velocity is available.

1 Introduction

Ocean mesoscale eddies, evolving in scales of 10s–100s of kilometers, represent the majority of the kinetic energy of the ocean circulation (Ferrari & Wunsch, 2009). Stirring by mesoscale eddies plays an important role in the transport and mixing of oceanic tracers, which impacts ocean dynamics (Hallberg & Gnanadesikan, 2006; J. Marshall & Radko, 2003, 2006; Wolfe & Cessi, 2009, 2010) and biogeochemistry (Steinberg et al., 2019; McGillicuddy Jr et al., 2003; Siegenthaler, 1983; Gnanadesikan et al., 2015). The ocean components of most climate models are of insufficient resolution to resolve mesoscale eddies and their impact on tracer stirring has to be parameterized. The commonly-used parameterization in ocean models mimics two aspects of the mesoscale eddy stirring: the advection of buoyancy or thickness to flatten isopycnals ('GM', Gent & Mcwilliams, 1990; Gent et al., 1995) and diffusion of tracers along isopycnals to reduce mean tracer variance ('Redi', Redi, 1982). These two schemes can be formulated as a single rank-three diffusivity tensor with its symmetric part representing the Redi scheme and its antisymmetric part representing the GM scheme (Griffies, 1998). Model simulations are sensitive to the magnitude and distribution of the coefficients of both the GM and Redi parameterizations (J. Marshall & Radko, 2003; Gnanadesikan et al., 2015; J. Marshall et

al., 2017; Jones & Abernathey, 2019), and so these coefficients must be constrained by physical insight or measurement. Many theoretical studies have focused on the GM coefficient (e.g., Visbeck et al., 1997; Cessi, 2008; D. P. Marshall & Adcroft, 2010; D. P. Marshall et al., 2012; Jansen et al., 2015), leaving the constraints on the Redi coefficient less well understood.

Observational studies have estimated the isopycnal tracer diffusivity (i.e., the Redi coefficient) using satellite (J. Marshall et al., 2006; Ferrari & Nikurashin, 2010; R. P. Abernathey & Marshall, 2013) and *in situ* data (Zhurbas & Oh, 2003; Zhurbas et al., 2014; Cole et al., 2015; Groeskamp et al., 2017; Roach et al., 2018), but direct observations of the full-depth diffusivity is only available at two sites: one in the North Atlantic (Ledwell et al., 1998) and one in the Southern Ocean (Tulloch et al., 2014). Studies have inferred the vertical structure of diffusivity based on the mixing length theory (MLT, Prandtl, 1925) and variations that account for mean flow suppression (suppressed mixing length theory or SMLT, Ferrari & Nikurashin, 2010; Klocker et al., 2012). The SMLT prediction for the diffusivity, κ_{SMLT}, is

$$\kappa_{\mathrm{SMLT}} = \frac{u_{\mathrm{rms}} L}{1 + [\frac{\tau}{L}(c_w - \bar{u})]^2}, \tag{1}$$

where u_{rms} is the rms eddy velocity, L is the "unsuppressed" mixing length (i.e., the mixing length without mean flow suppression effects), τ is the eddy decorrelation time scale, c_w is the zonal eddy phase speed, and $\bar{u}$ is the mean flow. While the essence of SMLT is captured by (1), other versions exist with dimensional parameters replaced by equivalent dimensional parameters or which differ from (1) by the appearance of nondimensional constants of order one. In the present case, the mixing efficiency often included in expressions like (1) (e.g., Ferrari & Nikurashin, 2010; Klocker & Abernathey, 2014) has been absorbed into L.

Despite the wide use of MLT and SMLT in ocean studies, its applicability to estimating full-depth diffusivity profiles is still unclear. Assumptions about the form of the unsuppressed mixing length, L, vary from study to study. Some studies assume that L is depth-independent and is given either the observed eddy length scale (Bates et al., 2014) or the local Rossby deformation radius (Groeskamp et al., 2020; Wei & Wang, 2021). This assumption leads to a vertical structure of the diffusivity that is controlled by the vertical structure of the rms eddy velocity and mean flow. Other studies assume that L has a vertical structure, which is estimated from the Eulerian tracer variance (Cole et al., 2015) or Lagrangian particle dispersion (Klocker et al., 2012; Griesel et al., 2014; Wolfram & Ringler, 2017). Such an assumption makes predicting of the vertical structure of diffusivity challenging since there is no *a priori* theory that predicts the vertical structure of these quantities.

On the other hand, the studies mentioned above tend to estimate the diffusivity as a scalar, either by assuming that mixing is isotropic or by only estimating the cross-stream diffusivity (e.g., Ferrari & Nikurashin, 2010; R. Abernathey et al., 2013; Groeskamp et al., 2020). However, the isopycnal mixing in the ocean has been revealed to be broadly anisotropic (e.g., Rypina et al., 2012; Fox-Kemper et al., 2013; S. D. Bachman et al., 2020), and the mixing is better described by a diffusivity tensor (Fox-Kemper et al., 2013). Accounting for the anisotropy of the mixing is important for accurate representation of the eddy transport in parameterizations (R. D. Smith & Gent, 2004; S. D. Bachman et al., 2020; Stanley et al., 2020). Both Eulerian (S. Bachman & Fox-Kemper, 2013; Fox-Kemper et al., 2013; S. D. Bachman et al., 2015, 2020) and Lagrangian (Rypina et al., 2012; Kamenkovich et al., 2015; Wolfram et al., 2015; Chen & Waterman, 2017) methods have been used to estimate the anisotropy of the mixing, and these estimates are usually consistent (Fox-Kemper et al., 2013). A consequence of this anisotropy is that mixing is typically much stronger in the direction of the mean flow than across it (S. D. Bachman et al., 2020), which could be due to the enhancement of along-stream mixing by mean flow shear (K. S. Smith, 2005, 2007a) and the suppression of cross-stream mixing by eddy prop-

agation relative to the mean flow (Ferrari & Nikurashin, 2010; Klocker et al., 2012). A complete parameterization accounting for this anisotropy requires understanding the scaling of both along- and cross-stream diffusivities.

The vertical structure of tracer diffusivity tensor was recently examined by S. D. Bachman et al. (2020). They proposed an anisotropic parameterization in which the cross-stream diffusivity is equal to the GM diffusivity and ratio of the along-stream to the cross-stream diffusivity is randomly selected from an exponential distribution. This parameterization compared favorably to the vertical profile of the global horizontal average of the diffusivity diagnosed from a high-resolution global ocean model using a multiple tracer inversion method. However, the physical meaning of this comparison is unclear, since multiplying an averaged diffusivity by an averaged gradient does not necessarily recover the averaged flux. The vertical structure of eddies is dependant on local baroclinic instability (K. S. Smith, 2007a; Tulloch et al., 2011), and the vertical structure of the cross-stream diffusivity is even more complex due to mean flow suppression in regions with differing dynamics (Bates et al., 2014; Klocker & Abernathey, 2014; Cole et al., 2015; Groeskamp et al., 2020). The extent to which extant scaling theories for isopycnal mixing account for this local variability has not been thoroughly studied.

In this study we attempt to address whether MLT and SMLT adequately describe the vertical variation and anisotropy of tracer diffusivities and whether the mixing length is depth-independent.This study considers—in a point-wise manner—the vertical structure of the isopycnal diffusivity in an idealized basin circulation model, which contains multiple gyres, western boundary currents and a circumpolar current like the Antarctic Circumpolar Current. The 3D diffusivity tensor is diagnosed using the multiple tracer inversion method of S. D. Bachman et al. (2015) to provide a "ground truth" for comparison to scaling theories for the along- and cross-stream diffusivities. This study verifies MLT and SMLT scaling in the upper ocean, but also finds that the mixing regime is distinctly different below the thermocline. Here, the diffusivity scales like the eddy kinetic energy times a depth-independent mixing time. The difference between these mixing regimes is attributed to the dominance by the nonlinear and linear processes in the upper and deep ocean, respectively. We propose an improved theory which combines the effects of both nonlinear and linear mixing processes.

The rest manuscript is organized as follows. Section 2 introduces the configuration of the numerical model and the multiple tracer inversion method used to diagnose the diffusivity tensor. Section 3 describes the overall properties of the magnitude and orientation of the eigenvalues and eigenvectors of the symmetric part of the diffusivity tensor and their vertical structures. The full-depth scaling of the along- and cross-stream diffusivities (first two eigenvalues) in four different regions is discussed in section 4. Section 5 offers a summary and conclusions.

2 Approach

2.1 Idealized basin circulation model

This study uses an idealized configuration of Massachusetts Institute of Technology general circulation model (MITgcm, J. Marshall, Adcroft, et al., 1997; J. Marshall, Hill, et al., 1997; Campin et al., 2020) used by several previous studies (Wolfe et al., 2008; Cessi & Wolfe, 2009; Wolfe & Cessi, 2009, 2010, 2011; Cessi et al., 2010; Wolfe, 2014). The model is formulated in a two-hemisphere basin on an equatorial β-plane ($\beta = 2.3\times 10^{-11}$ m^{-1}s^{-1}) with a flat bottom. The model domain has width $W = 2440$ km in zonal direction, length $L = 9880$ km in meridional direction and a uniform depth $H = 2440$ m, with no-slip vertical walls on the boundary, except for the southern eighth of the domain, where the flow is zonally reentrant (figure 1). The horizontal resolution is 5.4 km, resolving the first baroclinic deformation radius at every latitude. The vertical grid spac-

ing varies from 13 m at the surface to 274 m at the bottom with a total of 20 vertical levels.

The model is forced by zonally uniform zonal winds and a relaxation to a zonally uniform surface temperature distribution, an idealization of the forcing in the Atlantic Ocean. The dissipation is provided by the horizontal Laplacian viscosity ($A_h = 12$ m^2 s^{-1}), horizontal biharmonic viscosity ($A_4 = 9 \times 10^8$ m^4 s^{-1}), vertical viscosity ($A_v = 3 \times 10^{-4}$ m^2 s^{-1}), and linear bottom drag ($r = 1.1 \times 10^{-3}$ m s^{-1}). Buoyancy is a linear function of temperature only, which is advected using a seventh-order monotonicity-preserving scheme (Daru & Tenaud, 2004) and diffused with a constant isotropic diffusivity ($\kappa = 4.9{\times}10^{-5}$ m^2 s^{-1}) in both horizontal and vertical directions. Figure 1a shows the mean surface flow fields in the model. The model contains multiple gyres, boundary currents, and a zonally reentrant channel flow analogous to the Antarctic Circumpolar Current. Figure 1b gives a snapshot of the surface vorticity and sea surface height anomaly fields, which shows rich eddy fields coexisting with the mean circulations.

2.2 Diagnosing the diffusivity tensor based on a tracer-based inversion method

The nine-component diffusivity tensor is diagnosed using a tracer-based inversion method of S. D. Bachman et al. (2015, 2020), which is used as the "ground truth" to test against the existing scaling theories. An advantage of this method is that it accounts for the anisotropy of the eddy diffusion by diagnosing each component of a diffusivity tensor using multiple tracers, rather than simply calculating a scalar diffusivity based on the flux-gradient relationship of a single tracer. At least three different tracers are required to uniquely solve for the nine components of the diffusivity tensor, but to reduce the noise and bias due to the choice of tracers we use more than three tracers to overdetermine the diffusivity tensor and solve for the diffusivity using a least squares method (S. D. Bachman et al., 2015, 2020).

A total of 27 passive tracers, C_α, are advected with the velocity field of the model according to

$$\frac{\mathrm{D}C_\alpha}{\mathrm{D}t} = \lambda_\alpha \left(C_\alpha^0 - C_\alpha \right), \tag{2}$$

where λ_α is the relaxation rate and C_α^0 is the initial condition of α^{th} tracer. The 27 tracers are divided into 3 sets; each set is relaxed to the initial conditions with relaxation time scales of 1 year for tracers 1-9, 3 years for tracers 10-18, and 9 years for tracers 19-27. There are 9 different initial conditions,

$$\begin{aligned}
&C^0_{1,10,19} = \frac{y}{L}, && C^0_{2,11,20} = \sin\frac{\pi y}{L}, && C^0_{3,12,21} = \cos\frac{\pi y}{L},\\
&C^0_{4,13,22} = \sin\frac{2\pi x}{W}, && C^0_{5,14,23} = \cos\frac{2\pi x}{W}, && C^0_{6,15,24} = \sin^2\frac{\pi x}{W},\\
&C^0_{7,16,25} = \frac{H-2z}{H}, && C^0_{8,17,26} = \cos\frac{\pi z}{H}, && C^0_{9,18,27} = \sin\frac{2\pi z}{H},
\end{aligned} \tag{3}$$

The 3D eddy diffusivity tensor is diagnosed by inverting the flux-gradient relationship, so

$$\mathbf{K} = -\overline{\boldsymbol{u}'\boldsymbol{C}'} \left[\nabla \bar{\boldsymbol{C}} \right]^\dagger, \tag{4}$$

where $\mathbf{K}$ is the diffusivity tensor, $\boldsymbol{C}$ is a row vector of the 27 tracers, $\overline{(\cdot)}$ is a 20-year and 152-km spatial average, and $(\cdot)^\dagger$ denotes the Moore-Penrose pseudoinverse (Moore, 1920; Penrose, 1955). We solve for $\mathbf{K}$ in a least squares sense using all 27 tracers, which can significantly reduce random errors due to the choice of a particular set of tracers (S. D. Bachman et al., 2015).

To test the effectiveness of this method, one of the 27 tracers is withheld from the inversion calculation, and the flux of the withheld tracer is reconstructed using the diffusivity tensor, $\mathbf{K}_w$, diagnosed from the other 26 tracers. Following S. D. Bachman et

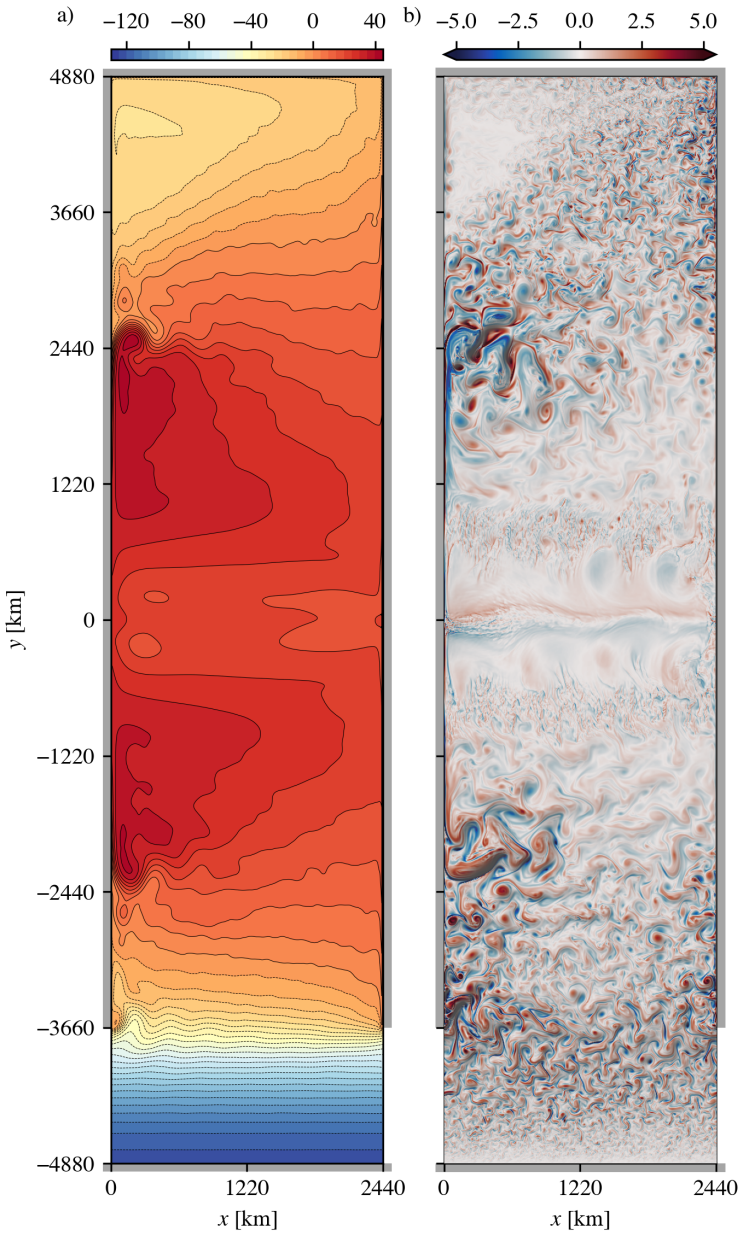

Figure 1. (a) Mean sea surface height fields in centimeters from the idealized eddy-resolving basin model. The contour interval is 5 cm. (b) Snapshot of the instantaneous surface layer vorticity in 10^{-5} s^{-1} (colors) and sea surface height in centimeters (shading) from the same model. The shading around the edges are the walls on the boundary. There is a channel in the southmost eighth of the domain.

al. (2020) the relative error of reconstructed tracer flux is estimated as

$$\epsilon = \frac{|\overline{\boldsymbol{u}'C'_w} + \mathbf{K}_w \nabla \bar{C}_w|}{|\overline{\boldsymbol{u}'C'_w}|}, \tag{5}$$

where C_w is the tracer that is withheld from the tracer inversion.

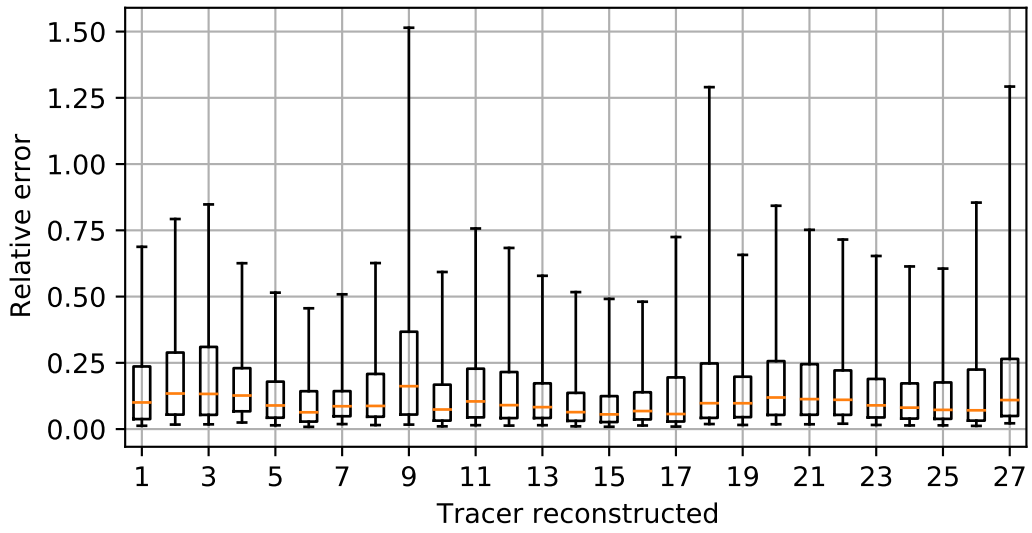

Figure 2. Boxplot for the point-wise relative error of the reconstruction of the withheld tracer flux using the diagnosed diffusivity tensor. Each of the 27 tracers is withheld, and its flux is reconstructed using the diffusivity tensor diagnosed from the other 26 tracers. The labels on the x-axis indicate the tracer that is withheld from the tracer inversion.

Each of the 27 tracers is withheld from the tracer inversion to estimate the relative error of reconstructing their fluxes—the results are shown in figure 2. The relative error is generally small, with a median smaller than 0.2, so the diffusivity tensor captures most characteristics of the tracer transport. The reconstruction is not very different for tracers with different initial distributions, except tracers C_9, C_{18} and C_{27}. These tracer have a large initial vertical gradient and the largest relative error, but the reconstruction of their fluxes is still satisfactory. The relative errors for tracers relaxed at different rates are similar, so the reconstruction is not very sensitive to the relaxation rate. We also tried to use fewer tracers (e.g. only using tracers 1–9) to do the inversion, and the relative error is again not very different from the inversion using all 27 tracers (not shown), which suggests that 9 tracers with distinct initial distributions are likely sufficient to diagnose the diffusivity tensor. In the later results we simply used the diffusivity tensor $\mathbf{K}$ diagnosed using all the 27 tracers.

3 Eigendecomposition of the symmetric diffusivity tensor

3.1 Anisotropy and orientation of the mixing

The diffusivity tensor can be decomposed into a sum of a symmetric and antisymmetric tensors,

$$\mathbf{K} = \mathbf{S} + \mathbf{A}. \tag{6}$$

The antisymmetric tensor, $\mathbf{A}$, gives a skew tracer flux (Griffies, 1998) and behaves like a bolus velocity (Gent et al., 1995). This tensor represents the release of mean poten-

tial energy by baroclinic instability and is important for ocean dynamics but has no contribution to the tracer variance budget. In contrast, the symmetric tensor, $\mathbf{S}$, determines the diffusive transport of tracers and, if positive definite, decreases the resolved tracer variance. This work aims to study the properties of the tracer diffusion so focuses on the symmetric tensor, while the antisymmetric tensor will be investigated in the future work.

The symmetric tensor $\mathbf{S}$ can be diagonalized as

$$\mathbf{S}\boldsymbol{\varphi}_i = \kappa_i \boldsymbol{\varphi}_i, \tag{7}$$

where κ_i $(i = 1, 2, 3)$ are the three eigenvalues along the corresponding eigenvectors, $\boldsymbol{\varphi}_i$ $(i = 1, 2, 3)$, which indicate the three orthogonal principal directions of the mixing.

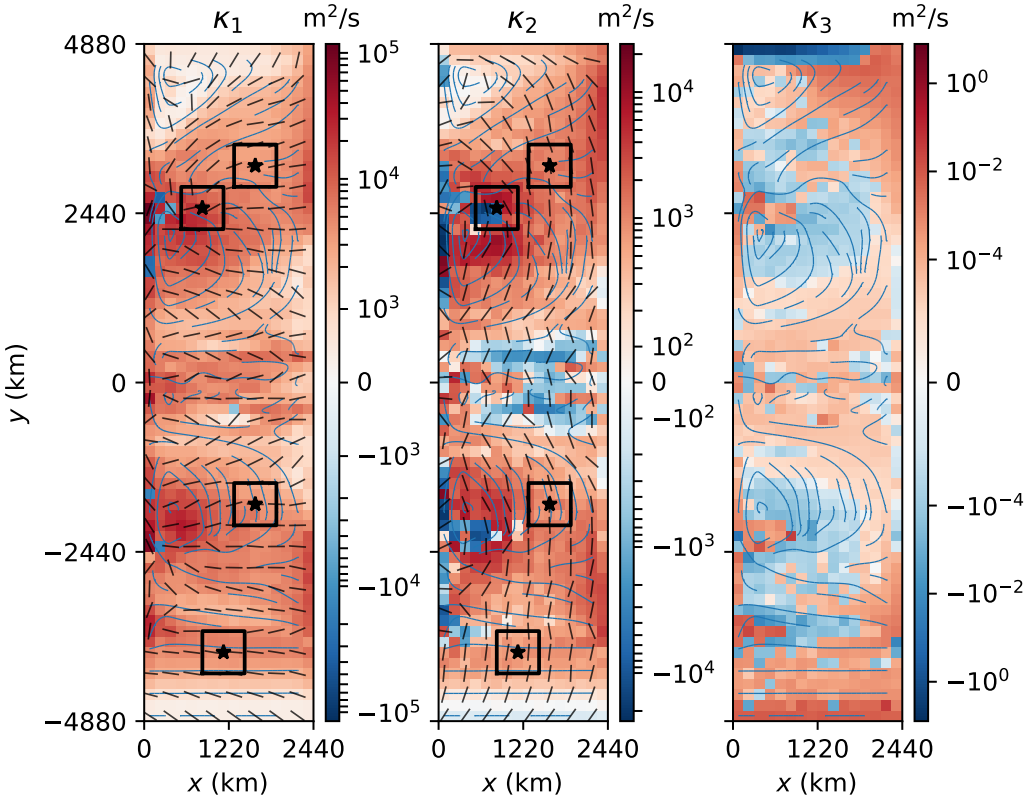

Figure 3. Eigenvalues for the symmetric part of the diffusivity tensor at 138 m depth as a example. Black lines indicate the horizontal direction of the corresponding eigenvectors. The last eigenvalue κ_3 is almost vertical, so the horizontal components of its eigenvector is small. Blue lines are the mean flow streamlines. Black boxes are the regions where the vertical structures of the diffusivities are analyzed. Black stars indicate the locations where the scaling for the vertical structure of diffusivity is examined.

The horizontal distribution of the three eigenvalues at 138 m depth is shown in figure 3. The first two eigenvalues, κ_1 and κ_2, are nearly horizontal and much larger than the third eigenvalue, κ_3, which is almost vertical. Figure 4a shows the histogram for the angles between the direction of each eigenvector and the buoyancy gradient. The directions of κ_1 and κ_2 are nearly along the isopycnals (i.e., are epipycnal), while the direction of κ_3 is predominantly diapycnal. The epipycnal diffusion by mesoscale eddies plays

an important role in tracer transport along isopycnals, which have been widely investigated in oceanic observations (e.g., Stammer, 1998; Zhurbas & Oh, 2003, 2004; J. Marshall et al., 2006; R. P. Abernathey & Marshall, 2013; Cole et al., 2015; Groeskamp et al., 2017; Roach et al., 2018) and is also the focus of this study. The diapycnal mixing, although is very important, is more likely to be induced by submesoscale or microscale processes which are not resolved in this model.

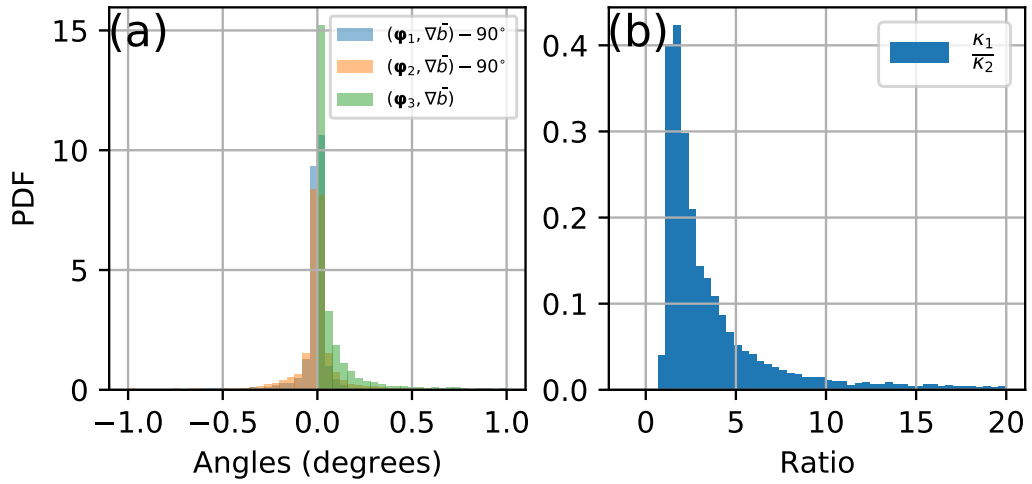

Figure 4. (a) Probability distribution function of the angles of the three eigenvectors relative to the isopycnals. Blue and orange bars show the angles for the first and second eigenvectors, $\boldsymbol{\varphi}_1$ and $\boldsymbol{\varphi}_2$, respectively, relative to the isopycnals. Green bars show the angles between the third eigenvector, $\boldsymbol{\varphi}_3$, and the buoyancy gradient. (b) Probability distribution function of the ratio of the major to the minor diffusivities.

The magnitude of κ_1 is 2–3 times larger than κ_2 on average (figure 4b), indicating weak anisotropy for the along-isopycnal mixing. Hereafter κ_1 and κ_2 will be denoted as the major and minor isopycnal diffusivities, respectively. The horizontal direction of the major diffusivity κ_1 is mostly along the mean flow, with an exception in the subtropical gyres, while the direction of the minor diffusivity κ_2 is mostly across the mean flow, orthogonal to the major diffusivity (figure 3; see also figure 6). Negative values of diffusivity exist in both the major and minor diffusivities, and are mostly found in the equatorial current regions, western boundary current and its extensions, and the northwest corner of the circumpolar current (figure 3). In these regions the advection of tracer variance by mean flow is significant and can be either upgradient or downgradient. This can be understood by considering the tracer variance budget,

$$\frac{\partial}{\partial t}\frac{\overline{C'^2}}{2} + \nabla\cdot\left(\overline{\boldsymbol{u}\frac{C'^2}{2}}\right) + \overline{\boldsymbol{u}'C'}\cdot\nabla\bar{C} = \overline{C'\mathcal{D}'} + \overline{C'\mathcal{S}'}, \tag{8}$$

where $\overline{C'^2}/2$ is the tracer variance, $\mathcal{D}$ represents dissipation, and $\mathcal{S}$ represent sources (i.e., relaxation). Assuming a statistically steady state with weak relaxation and invoking the flux-gradient parameterization of the eddy fluxes, the tracer variance budget becomes

$$\nabla\cdot\left(\overline{\boldsymbol{u}\frac{C'^2}{2}}\right) - \nabla\bar{C}\cdot\mathbf{S}\cdot\nabla\bar{C} \approx \overline{C'\mathcal{D}'} < 0, \tag{9}$$

where the less-than sign emphasizes that dissipation is a sink of tracer variance. The sign of the diagradient flux term, $\nabla\bar{C}\cdot\mathbf{S}\cdot\nabla\bar{C}$, depends on the signs of the eigenvalues of $\mathbf{S}$

(i.e., the diffusivities). This term is positive- (negative-) definite if all the diffusivities are positive (negative); otherwise it is sign-indefinite. If advection of tracer variance (first term on the LHS of (9)) is negligible or divergent, the cross-gradient term—and thus the diffusivities—must be positive to balance dissipation. On the other hand, significant convergent variance advection can overwhelm dissipation and negative diffusivities are required to balance the sum of advection and dissipation. A detailed study on the dynamics in these regions will be pursued in the forthcoming work.

3.2 Vertical structure of the isopycnal diffusivities

The vertical structure of the isopycnal diffusivity is less well understood than the horizontal structure due to the sparsity of full-depth observations (Groeskamp et al., 2020). It is thought that the vertical structure of eddies and mixing is different at locations with differing dynamics (K. S. Smith, 2007b; Tulloch et al., 2011; K. S. Smith & Marshall, 2009). This study seeks to relate the vertical structure of the diffusivity to the dynamical properties in four typical regions with different dynamics: the circumpolar current, subtropical gyre, western boundary current, and transition between subtropical and subpolar gyres (shown by the black boxes from south to north in figure 3). The vertical profiles of the first two eigenvalues are analyzed in 600 km $\times$ 600 km boxes (black boxes in figure 3) in the four regions.

The vertical structures of the magnitude of κ_1 and κ_2 in these four regions are shown in figure 5. The vertical structures of diffusivities are generally consistent in each region, except in the western boundary current where the local variation is large. The horizontal distribution of diffusivities in the western boundary current is complicated by the stability of the jets, wave radiation and formation of recirculations, which can lead to both positive and negative diffusivities (Waterman & Jayne, 2010; Chen & Waterman, 2017). The magnitude of κ_1 is generally several times larger than κ_2, especially near the surface (figure 5), indicating strong anisotropy there. The major diffusivity, κ_1, decreases monotonically with depth, except in some levels near the surface, while the minor diffusivity, κ_2, tends to have a subsurface maximum, which can reach to 1000 m in the circumpolar current and is shallower than 500 m depth in the other three regions. The cross-stream diffusivity in the Southern Ocean has also been observed to have a subsurface maximum (K. S. Smith & Marshall, 2009; R. Abernathey et al., 2010), which is explained to be due to the suppression of mixing by the mean flow (Ferrari & Nikurashin, 2010; Klocker et al., 2012). Since the direction of the minor diffusivity, κ_2, is mostly across the mean flow as well, we expect the vertical structure of κ_2 is affected by the mean flow suppression, which will be tested in the following section. The major diffusivity, κ_1, on the other hand, is mostly along the mean flow direction, which has been shown to be less impacted by the mean flow suppression than the cross-stream diffusivity (Riha & Eden, 2011; Griesel et al., 2014; Chen et al., 2014).

Figure 6 shows the vertical structure of the orientation of $\boldsymbol{\varphi}_1$ and $\boldsymbol{\varphi}_2$ in the four regions. The direction of $\boldsymbol{\varphi}_1$ ($\boldsymbol{\varphi}_2$) is generally along the zonal (meridional) direction in the upper levels of the four regions, and it is almost along (across) the direction of the mean flow above 1000 m in the four regions. In the deep levels $\boldsymbol{\varphi}_1$ is less aligned with the mean flow, perhaps because the mean flow is weak at depth (figure 7) and the interior PV gradient plays a more important role in the mixing direction (S. D. Bachman et al., 2020). In the subtropical gyre the direction of mean flow is not well-defined, because of the strong veering of the mean flow with depth (figure 7). In the circumpolar current the mixing directions veer from the mean flow direction at around 1000 m where magnitude of the major and minor diffusivities are similar. This might be be because the mean flow suppression is weaker at depth, so the mixing is close to isotropy, which means its direction is arbitrary.

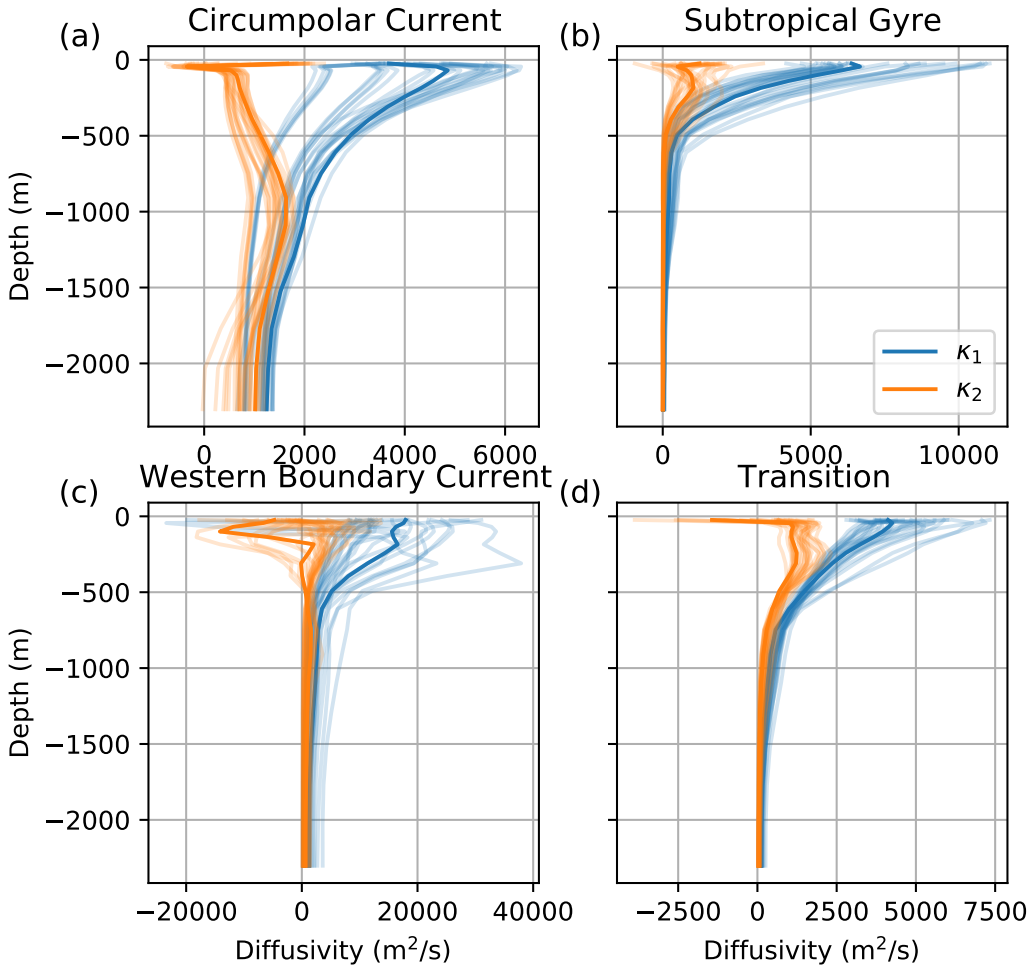

Figure 5. Vertical profiles of the isopycnal diffusivity in the four regions indicated by the black boxes in figure 3. The four regions from south to north are located in the (a) circumpolar current, (b) subtropical gyre, (c) western boundary current, and (d) transition between the subtropical and subpolar gyres. Bright color lines are the vertical profiles of the major diffusivity, κ_1, (blue) and minor diffusivity, κ_2, (orange) at the center of the four regions indicated by the black stars in figure 3. Shaded color lines give the vertical profiles of κ_1 (blue) and κ_2 (orange) at all grid points in the four regions.

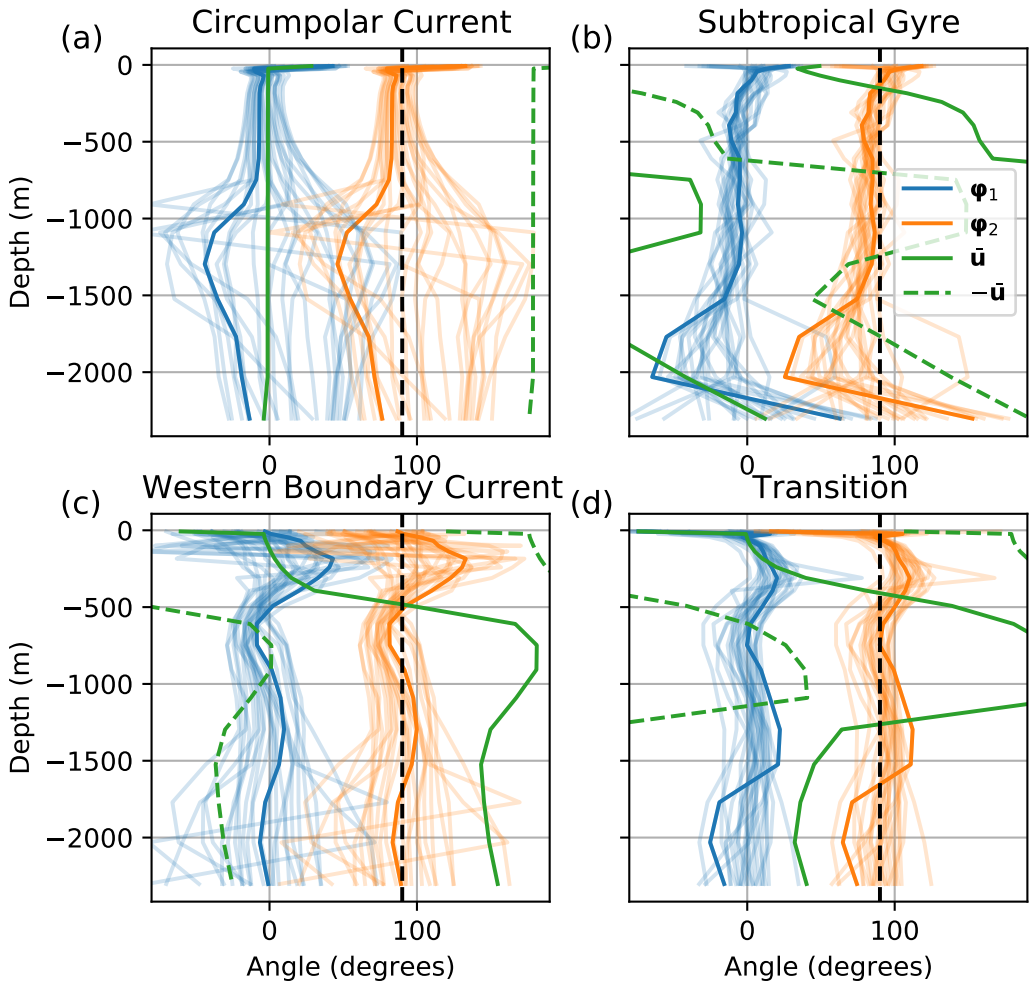

Figure 6. As in figure 5, but for the angles of the eigenvectors $\boldsymbol{\varphi}_1$ (blue line), $\boldsymbol{\varphi}_2$ (orange line) and the mean flow (green solid line) in degrees relative to the zonal direction. The direction opposite the mean flow (green dashed line) is also compared with the principal mixing directions since the eigenvectors are invariant under 180° rotations. The black dashed line indicates the meridional direction.

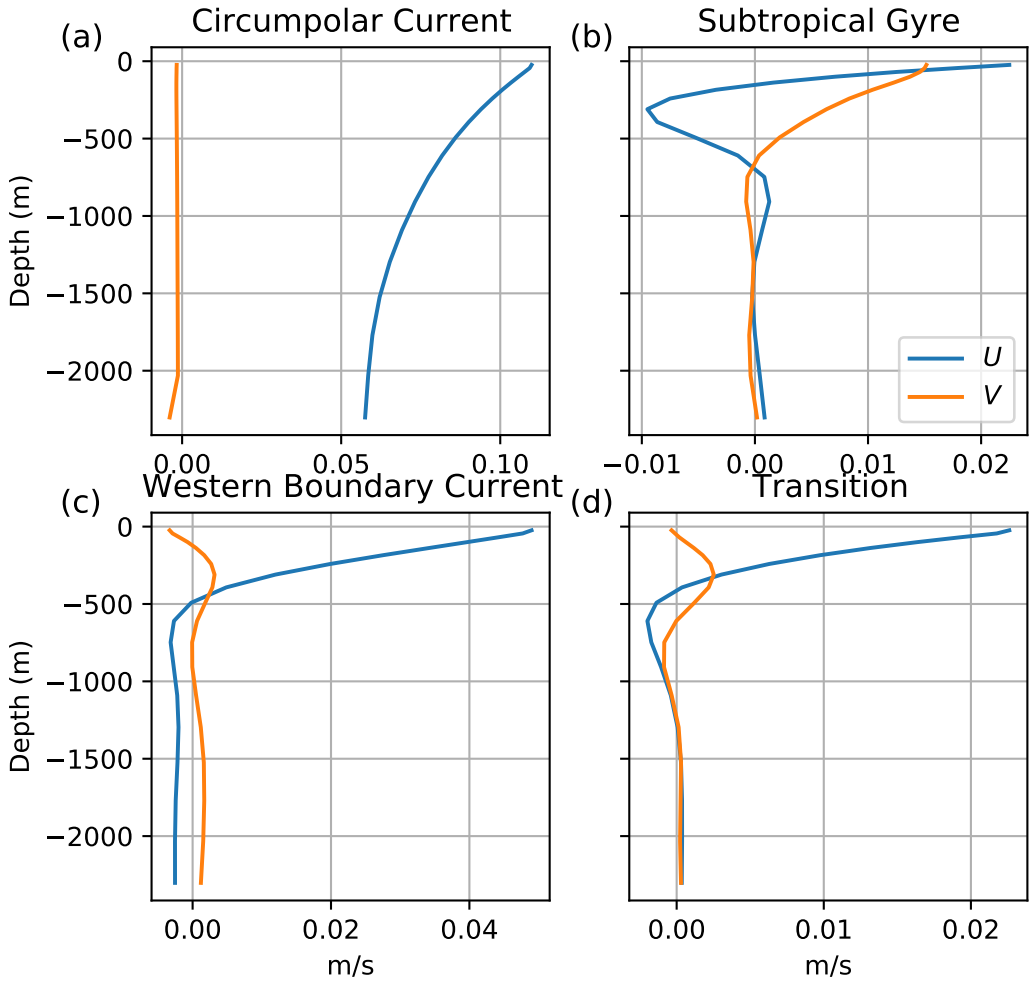

Figure 7. Vertical structure of the zonal (blue line) and meridional (orange line) mean flow velocity horizontally averaged over the same four regions as in figure 5. The surface velocity is not plotted because the surface meridional flow is dominated by the Ekman flow.

4 Scaling theories for the isopycnal diffusivities

The diffusivities, κ_1 and κ_2, determine tracer mixing along isopycnals, which has important impacts on the mean flow (Fox-Kemper et al., 2013; Bates et al., 2014; Chapman & Sallée, 2017; S. D. Bachman et al., 2020). Understanding the physical mechanism that gives rise to the anisotropy and vertical structure of these diffusivities can guide their parameterization in coarse-resolution models. Here we test the vertical structure of κ_1 and κ_2 against the existing scaling theories. Specific interest is attached to the source of the anisotropy of the isopycnal mixing and the applicability of MLT and SMLT to the full-depth scaling of diffusivities.

4.1 Source of the anisotropy

The major diffusivity, κ_1, is generally along the mean flow and is several times larger than the minor diffusivity, κ_2. What is the source of this anisotropy? Extant theories often suppose that along-stream mixing is dominated by shear-dispersion (Taylor, 1953; Young et al., 1982; K. S. Smith, 2005, 2007a), which leads to a diffusivity, κ_{SD}, as

$$\kappa_{\mathrm{SD}} \sim \frac{U^2 l_s^2}{\kappa_\perp}, \tag{10}$$

where U is a scale for the mean flow, l_s is the scale of the mean flow shear, and $\kappa_\perp$ is the cross-stream diffusivity. However, attempts to use (10) to scale κ_1 did not show good agreement (not shown), which suggests that shear dispersion is not playing a strong role in determining κ_1.

Another possible source of anisotropy is the suppression of cross-stream mixing by the mean flow, which is explained by steering level theory (Green, 1970; Killworth, 1997; K. S. Smith & Marshall, 2009; R. Abernathey et al., 2010; Ferrari & Nikurashin, 2010; Klocker et al., 2012; Bates et al., 2014; Chen et al., 2014; Pennel & Kamenkovich, 2014; Griesel et al., 2015; Balwada et al., 2016; Wolfram & Ringler, 2017; Chapman & Sallée, 2017; Groeskamp et al., 2020; Wei & Wang, 2021). The vertical structure of κ_2 at the center of the four regions (black stars in figure 3) is shown by the blue line in figure 8. It tends to have a subsurface maximum, which has also been observed for the cross-stream diffusivity in the Southern Ocean (K. S. Smith & Marshall, 2009; R. Abernathey et al., 2010) and is explained by SMLT (Ferrari & Nikurashin, 2010; Klocker et al., 2012; Bates et al., 2014). SMLT constructs the cross-stream diffusivity as a background eddy diffusivity times a suppression factor, F_s, defined as

$$\mathrm{F_s} = \frac{1}{1 + [\frac{\tau}{L}(c_w - \bar{u})]^2}, \tag{11}$$

which estimates the suppression of diffusivity due to the propagation of nonlinear eddies relative to the mean flow, where L, τ, c_w and $\bar{u}$ are as in (1).

The diagnosed cross-stream diffusivity, κ_2, is compared with the suppressed along-stream diffusivity, $\kappa_1 \mathrm{F}_s$, where $\bar{u}$ is obtained from the model ($\bar{u}$ is simply taken as the zonal mean flow since the direction of κ_2 is predominantly meridional (figure 6), but projecting the mean flow and eddy phase speed onto the direction perpendicular to $\boldsymbol{\varphi}_2$ gives similar results), and c_w is estimated following Klocker and Marshall (2014),

$$c_w = \bar{u}^z - \beta L_d^2, \tag{12}$$

where $\bar{u}^z$ is the depth-averaged zonal mean flow, and L_d is the Rossby deformation radius of the first baroclinic mode, calculated by solving a Sturm-Liouville problem for the baroclinic modes. The fit of $\kappa_1 \mathrm{F}_s$ to the profiles of κ_2 at the center of the four regions (black stars in figure 3) is shown by the orange solid line in figure 8, where the τ/L in (11) is treated as a single depth-independent parameter following Bates et al. (2014) and

obtained by least squares fitting, which minimizes the vertical integral of the squared difference between $\kappa_1 \mathrm{F}_s$ and κ_2 in each profile.

The suppressed major diffusivity, $\kappa_1 \mathrm{F}_s$, captures the vertical maximum and variation of κ_2 well in these regions, except in the western boundary current where negative values of diffusivity spoil the scaling. Indeed, $\kappa_1 \mathrm{F}_s$ provides a good model for κ_2 in most of the extra-tropics except near the boundaries, shown by the distribution of the point-wise misfit ratio evaluated for each vertical profile of κ_2, shown in figure A3a. This suggests that the along- and cross-stream diffusivities satisfy the same scalings, modulo suppression of cross-stream mixing by the mean flow. The anisotropy of the diagnosed isopycnal diffusion thus appears to be primarily due to the mean flow suppression effect.

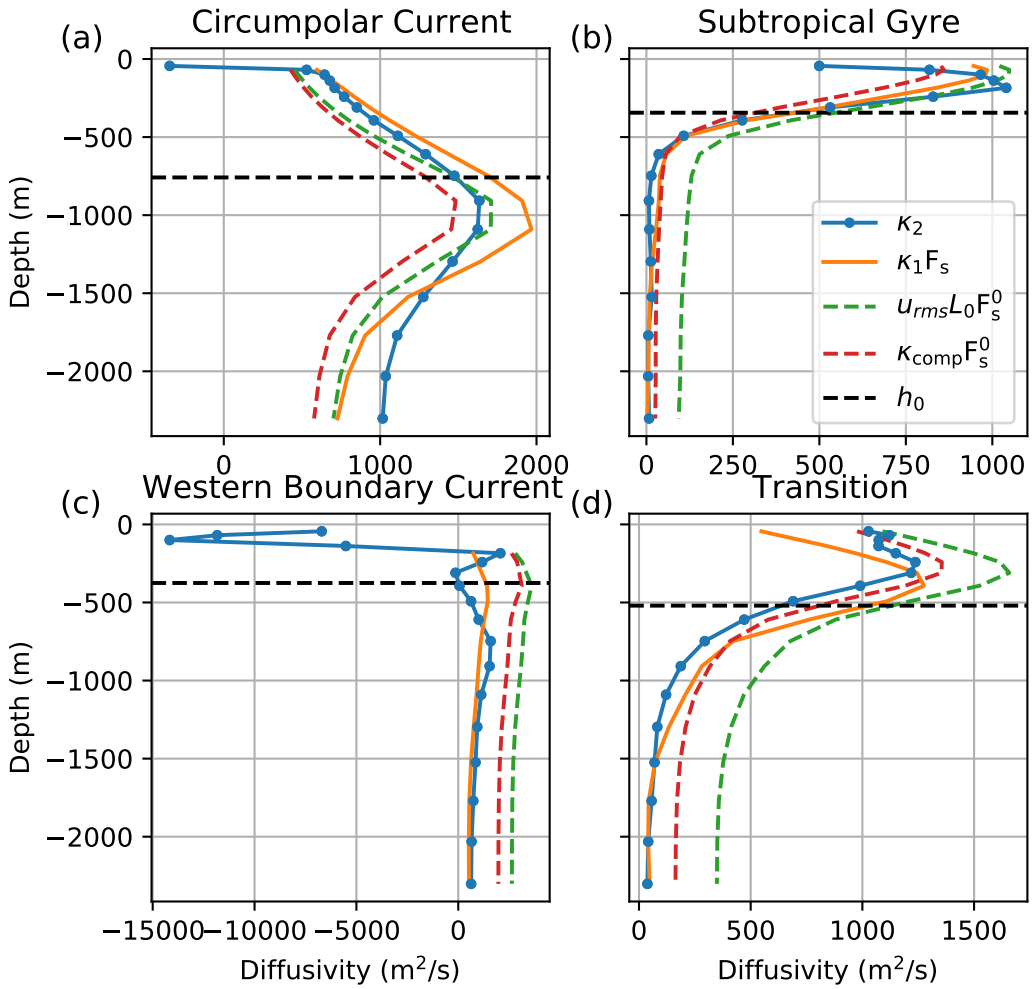

Figure 8. Scaling of the minor diffusivity, κ_2 (blue solid line with dots), at the center of the four regions, shown in figure 5. Orange lines show the fit for the vertical structure of κ_2 to the formula of $\kappa_1 \mathrm{F}_s$ (F_s expressed in (11)). Note that the negative values of of the diffusivity are excluded from the fit. The green and red dashed lines show the estimate with SMLT, $u_{\mathrm{rms}} L_0 \mathrm{F}_s^0$, and the suppressed composite scaling, $\kappa_{\mathrm{comp}} \mathrm{F}_s^0$, respectively, where the mixing length and time scales in the suppression factor F_s^0 is estimated as the energy containing scale, L_0, and a uniform decay time scale, $\tau_0 = 23$ days, respectively—see section 4.4. Black dashed line indicates the base of the thermocline, h_0.

4.2 Mixing length theory

Section 4.1 shows that the minor diffusivity, κ_2, can be reconstructed from the major diffusivity, κ_1. The major diffusivity therefore becomes the primary object of study. The vertical structure of κ_1 at the center of the four regions (black stars in figure 3) is shown in figure 9. The vertical structures of κ_1 and the rms eddy velocity are very similar, which suggests that κ_1 might follow a standard *un*suppressed MLT scaling with a depth-independent mixing length. In this case, the diffusivity is given by

$$\kappa_p(x, y, z) = u_{\rm rms}(x, y, z) L_{\rm mix}(x, y), \tag{13}$$

where $L_{\rm mix}$ is the mixing length and $u_{\rm rms}$ is the rms eddy velocity. For convenience, we refer to regimes described by (13) as in the "Prandtl regime" after Prandtl (1925), although Prandtl's theory was not restricted to depth-independent mixing lengths. Previous studies often include a nondimensional mixing efficiency in (13). We choose to absorb this constant into $L_{\rm mix}$.

The Prandtl regime, (13), is fitted to the vertical profiles of the major diffusivity at the center of the four regions, where $u_{\rm rms}$ is diagnosed from the model, and $L_{\rm mix}$ is obtained by least squares fitting, which minimizes the vertical integral of the squared difference between the major diffusivity, κ_1, and the prediction by the theories. The green solid line in figure 9 shows the fit of the major diffusivity κ_1 to the Prandtl regime (13). The Prandtl regime closely captures the vertical variation of κ_1 over full depth in the circumpolar current, while in the three basin regions, the Prandtl regime works well in the upper several hundred of meters but overestimates the diffusivity at depth. In the basin regions, Prandtl scaling appears to break down in the lower half of the thermocline, indicated by the dashed black line in figure 9 which is the stratification scale depth, h_0,

$$h_0 = \frac{\int z N^2 \, dz}{\int N^2 \, dz}, \tag{14}$$

where N is the Brunt-Väisällä frequency and the integrals are over the full depth of the ocean. This scale depth is a proxy for the base of the thermocline and would be equal to the e-folding depth of the thermocline if the stratification were exponential. In the three basin regions, the Prandtl regime (13) works well above h_0 but that (13) overestimates the diffusivity below h_0 in the three basin regions suggests that mixing below the thermocline may be controlled by different dynamics. Fits for κ_1 above h_0 are excellent in most of the extra-tropics (figure A1); the horizontal distribution of the fitted mixing length is given in figure A2.

While the upper-ocean diffusivity is well-modeled by MLT with a depth-independent mixing length, the question of what determines this mixing length remains. The mixing length scale is commonly compared to the scale of the energy containing eddies (Larichev & Held, 1995; Stammer, 1998; Ferrari & Nikurashin, 2010; Klocker & Abernathey, 2014), though the method to estimate this energy containing scale differs. Here we diagnose the energy containing scale from the peak of the surface EKE spectrum, similar to Larichev and Held (1995). Note that Larichev and Held (1995) used the barotropic energy spectrum, while we use the surface energy spectrum estimated using sea surface height (SSH) fields, which are more reflective to the baroclinic modes (Wunsch, 1997). In figure 10 we compared the fitted mixing length in (13) to the energy containing scales in the surface EKE spectrum, estimated using the instantaneous SSH fields over 20 years in the same box regions (black boxes in figure 3). The inverse of the fitted mixing length scale is close to the peak of the energy spectrum in all the four regions, which means the mixing length is approximately the energy containing scale. (Note that the energy-containing *scale* corresponds to the radius of the energy-containing eddies and so is approximately one-fourth the energy-containing *wavelength*, $2\pi/k$. The energy-containing scale is therefore approximately the inverse of the energy-containing wavenumber.) This motivates us to estimate

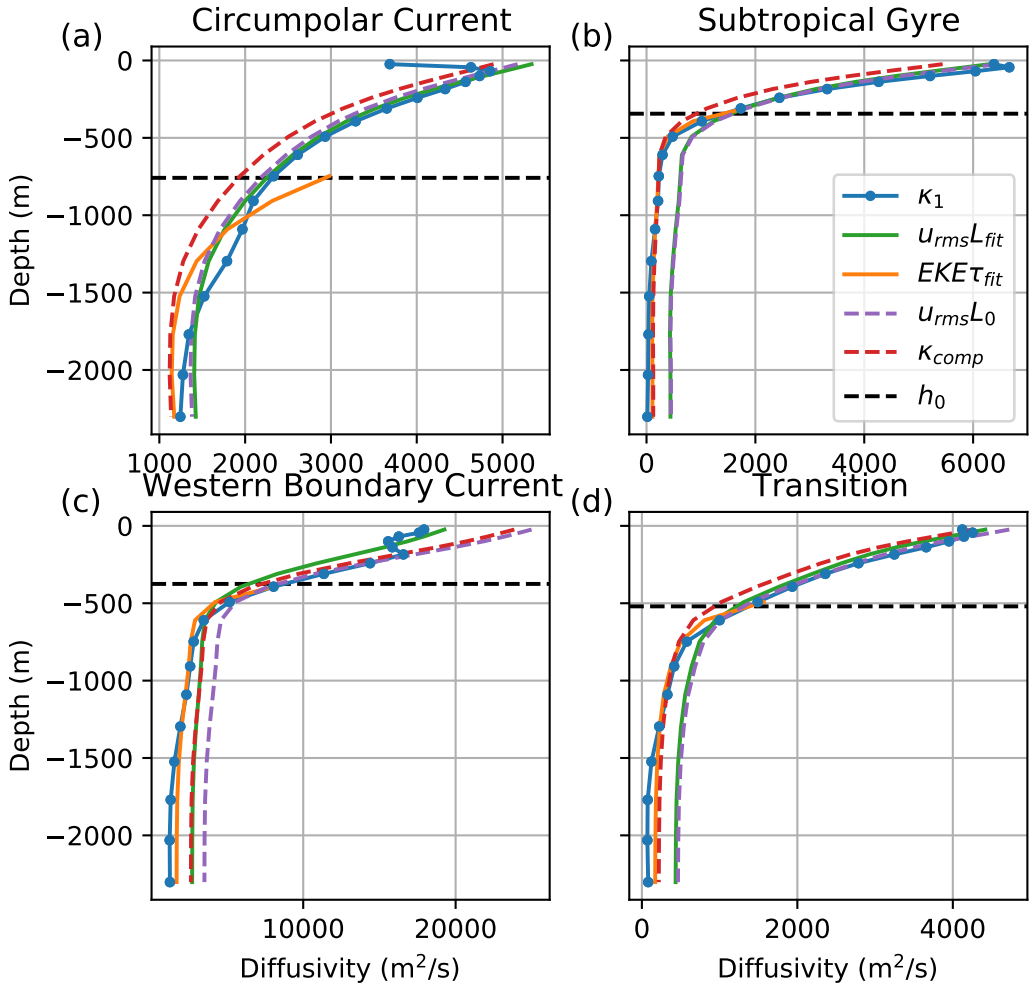

Figure 9. Scaling of the major diffusivity, κ_1 (blue solid line with dots), at the same locations as in figure 8. Green and orange solid lines show the fits of the vertical structure of κ_1 to Prandtl (13) and Taylor (16) regimes, respectively. Note that only the diffusivities below the base of the thermocline, h_0 (black dashed line), are fitted to the Taylor regime. Purple dashed line shows the scaling of Prandtl regime by estimating the mixing length as the energy containing scale, L_0. Red dashed line shows the composite scaling (20) by estimating the mixing length as the energy containing scale, L_0, and mixing time scale as a uniform constant, $\tau_0 = 23$ days—see section 4.4.

a mixing length scale, L_0, for the Prandtl scaling (13) as the inverse of the energy containing wavenumber,

$$L_0 = k_0^{-1}, \tag{15}$$

where k_0 is the energy containing wavenumber, which is estimated based on the surface EKE spectrum (dashed green line in figure 10). The scale L_0 is in the similar form as Larichev and Held (1995).

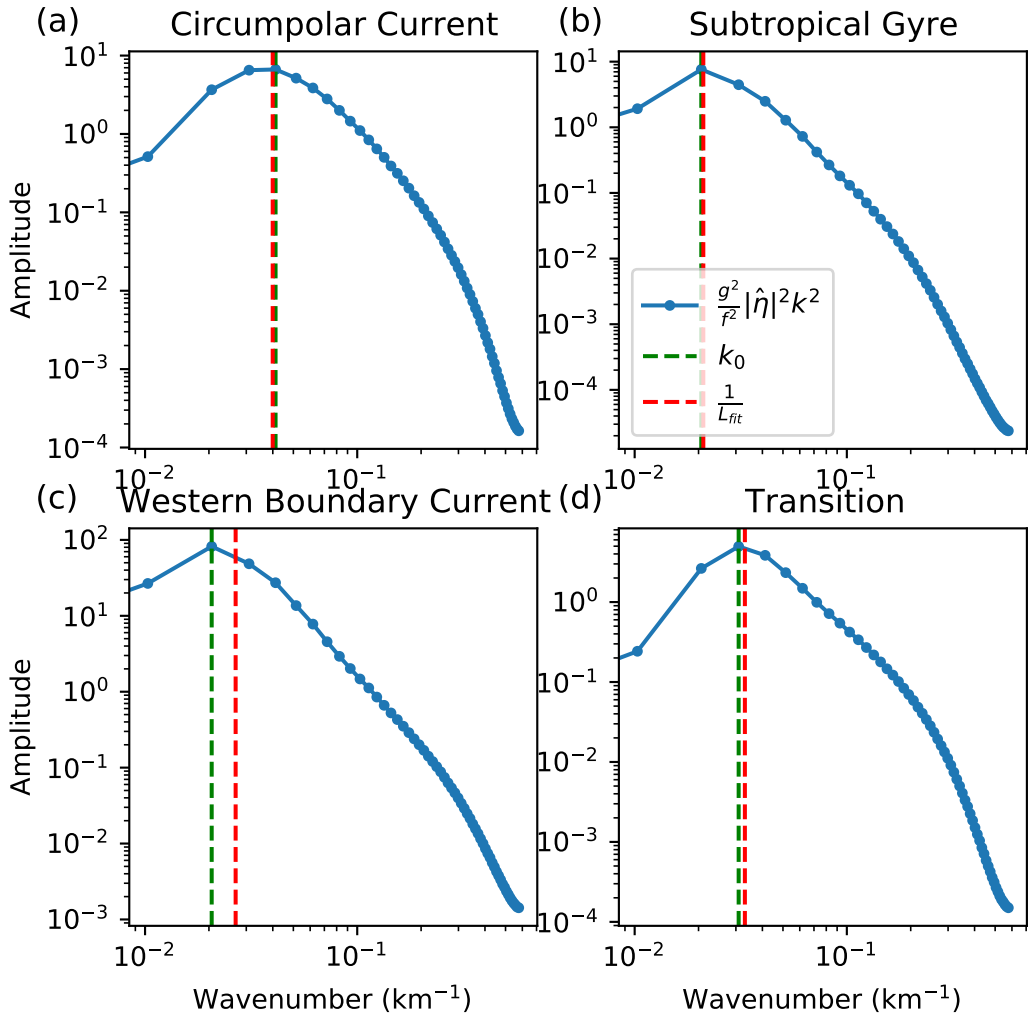

Figure 10. Surface kinetic energy spectrum (blue solid line with dots) calculated from the Fourier transform of sea surface height over the four regions in figure 5 and averaged over 20 years. The green dashed line indicates the energy containing wavenumber, k_0, and red dashed line is the inverse of the fitted mixing length from figure 9.

The purple dashed line in figure 9 shows the comparison between $u_{\text{rms}}L_0$ and κ_1. The scaling with L_0 matches the diffusivity in most of the regions, except that it slightly overestimates the mixing length in the western boundary current region. The energy containing scale of geostrophic turbulence is related to the inverse energy cascade due to nonlinear eddy-eddy interactions (Rhines, 1979; Haidvogel & Held, 1980). Barotropic eddy energy is injected at a scale close to the Rossby deformation radius, and then cascades to larger scales until the cascade is halted by, for example, friction or the planetary vor-

ticity gradient (Larichev & Held, 1995; Held & Larichev, 1996; Thompson & Young, 2006, 2007). In this study the mixing is clearly dominated by the nonlinear interactions in the circumpolar current and above the thermocline in the basin.

4.3 Mixing regime transition with depth

The Prandtl regime (13) models κ_1 well in the upper levels of the gyres, but overestimates the diffusivity below the thermocline because the diffusivity decreases with depth faster than the rms eddy velocity. Although the deep diffusivity is small, the mixing time scale is comparable to the mean flow advection time scale, so the mixing can still significantly impact deep water masses and circulation on climatological timescales. It is therefore worthwhile to pursue a more accurate expression for the deep diffusivity.

The vertical profile of diffusivity closely follows that of eddy kinetic energy (EKE) below the thermocline, which inspires us to test the expression for the diffusivity given by Taylor (1922), who wrote the diffusivity as a product of the eddy kinetic energy and a time scale. We assume the mixing time scale is depth-independent in this "Taylor regime," in which case the diffusivity is

$$\kappa_T(x,y,z) = \mathrm{EKE}(x,y,z)\tau_{\mathrm{mix}}(x,y), \tag{16}$$

where τ_{mix} is a mixing time scale and EKE is the eddy kinetic energy. The diffusivity in this Taylor regime follows the vertical structure of EKE, which is distinct from the vertical structure in the Prandtl regime (13).

The solid orange line in figure 9 shows the fit of the Taylor regime (16) to the major diffusivity, κ_1, below h_0. Below the thermocline (i.e., for $z < -h_0$), κ_1 follows the Taylor regime better than the Prandtl regime in the three basin regions. This indicates that there is a transition from the Prandtl regime to the Taylor regime at the base of the thermocline. This is supported by the point-wise misfit ratio evaluated for each vertical profile of κ_1, shown in figure A1. The value of the mixing time scale from the fit of (16) at each location is given in figure A2b. The mixing time scale is sort of uniform in the gyres, while it is smaller in the circumpolar current and tropics. The values in the gyres are generally close to the time scale for spin-down under the model's linear bottom drag, 25 days, which suggests that the mixing at deep levels might be controlled by the frictional damping. The diffusivity in the circumpolar current is well-described by the Prandtl regime over the full depth, so an estimate of the mixing time scale is not necessary there.

The mixing regime transition with depth is interpreted to be due to the transition from nonlinear to linear regimes from the upper to the deep ocean. The mixing length of the Prandtl regime in the upper ocean is close to the local energy-containing scale, which is associated with the inverse cascade due to nonlinear eddy-eddy interactions. The breakdown of the Prandtl regime in the deep ocean is likely because nonlinear interactions become weak below the thermocline and linear waves begin to dominate. The nonlinear and linear regimes can be distinguished by the nonlinearity parameter r, defined as the ratio of the rms eddy velocity to the propagation speed of coherent eddies (Chelton et al., 2007, 2011; Klocker et al., 2016) which are identified and tracked using 20 years of SSH snapshots and the same algorithm as Chelton et al. (2011) (see appendix Appendix B). More precisely,

$$r = \frac{\langle u_{\mathrm{rms}} \rangle}{c}, \tag{17}$$

where $c = \langle |\boldsymbol{u}_{\mathrm{coh}} - \langle \boldsymbol{u}_{\mathrm{coh}} \rangle| \rangle$ is the anomalous propagation speed of coherent eddies, $\boldsymbol{u}_{\mathrm{coh}}$ is their propagation velocity, and $\langle \cdot \rangle$ indicates the mean over eddies that are located in each of the four regions shown by the black boxes in figure 3. The mean propagation velocity of coherent eddies, $\langle \boldsymbol{u}_{\mathrm{coh}} \rangle$, is removed from the total velocity to maintain Galilean invariance. The rms eddy velocity, u_{rms}, is horizontally averaged in the same regions for

comparison with c. The linear and nonlinear regimes are determined by $r < 1$ and $r > 1$, respectively (Tulloch et al., 2009; Chelton et al., 2011; Klocker et al., 2016).

Figure 11 shows the vertical variation of r in the four regions. The parameter r decays rapidly with depth above the thermocline and then asymptotes to a value smaller than 1 below the thermocline in the three basin regions, while in the circumpolar current it is larger than 1 over full depth. Eddies in the circumpolar current region are nonlinear nearly over full depth, while in the other three regions nonlinear dynamics dominates above the thermocline and linear dynamics is more significant below it. A physical interpretation for this regime transition with depth is that the relative vorticity of eddies dominates in the upper levels so the PV contours can close in a circle, while in the deep levels the relative vorticity becomes weaker so the planetary vorticity gradient becomes important, which prevents the closure of PV contours and makes PV disturbances more wave-like. This regime transition impacts the vertical structure of mixing. The upper-ocean diffusivity due to nonlinear processes follows the vertical structure of rms eddy velocity, while the deep-level diffusivity is associated with the superposition of linear waves and follows the vertical structure of EKE. Parameterizations of full-depth mixing must account for this regime transition to produce the correct vertical structure of mixing.

Previous studies have found a transition from linear to nonlinear regime from tropics to midlatitude for the surface tracer mixing in the ocean, and the mixing in the nonlinear regime in midlatitudes is well-scaled by Prandtl MLT (Klocker & Abernathey, 2014; Klocker et al., 2016). A similar transition is shown in figure A1a, which shows that the Prandtl regime characterizes upper-ocean mixing in the extra-tropics, but not in the tropics. This study further suggests that such regime transition also happens with depth in the midlatitude ocean, and the mixing in linear regime in fact is better characterized by the Taylor regime. The Taylor regime also works for mixing below the thermocline in the tropics shown in figure A1b.

4.4 A composite scaling theory for the full-depth diffusivity

The scaling of the major diffusivity, κ_1 shows that the Prandtl regime (13) only works well in the upper level in the gyres, while deep mixing follows the Taylor regime (16). The minor diffusivity, κ_2, can be recovered from the major diffusivity, κ_1, after multiplication by the mean flow suppression factor (11), so the scaling for the minor diffusivity should account for the same mixing regime transition as well. To account for both Prandtl and Taylor regimes in the scaling of the diffusivity, we seek a generalized formula that can smoothly transition from the Prandtl regime to the Taylor regime.

In the original form of SMLT (Ferrari & Nikurashin, 2010), the unsuppressed diffusivity, κ_u, is

$$\kappa_u = \gamma^{-1}\mathrm{EKE}, \tag{18}$$

where γ is the decorrelation rate. Ferrari and Nikurashin (2010) estimates γ as an eddy turnover rate, u_{rms}/L_0, where L_0 is the inverse energy-containing wavenumber, defined in (15). Adopting this into (18), κ_u becomes $u_{\mathrm{rms}}L_0$, which is MLT and the numerator in SMLT (1). MLT assumes that the mixing is controlled by nonlinear eddy-eddy interactions; however, this is not the case in the deep ocean in the basin, where linear wave dynamics is more important. The steering level theory based on linear stability analysis (K. S. Smith & Marshall, 2009; Griesel et al., 2015) produces a similar scaling as SMLT, but it estimates γ as the growth rate of linearly unstable waves, which makes (18) a depth-independent time scale times the EKE, as in the Taylor regime.

To account for both the nonlinear and linear regimes, we assume that γ has contributions from both the eddy turnover rate, u_{rms}/L_0, and a depth-independent decay

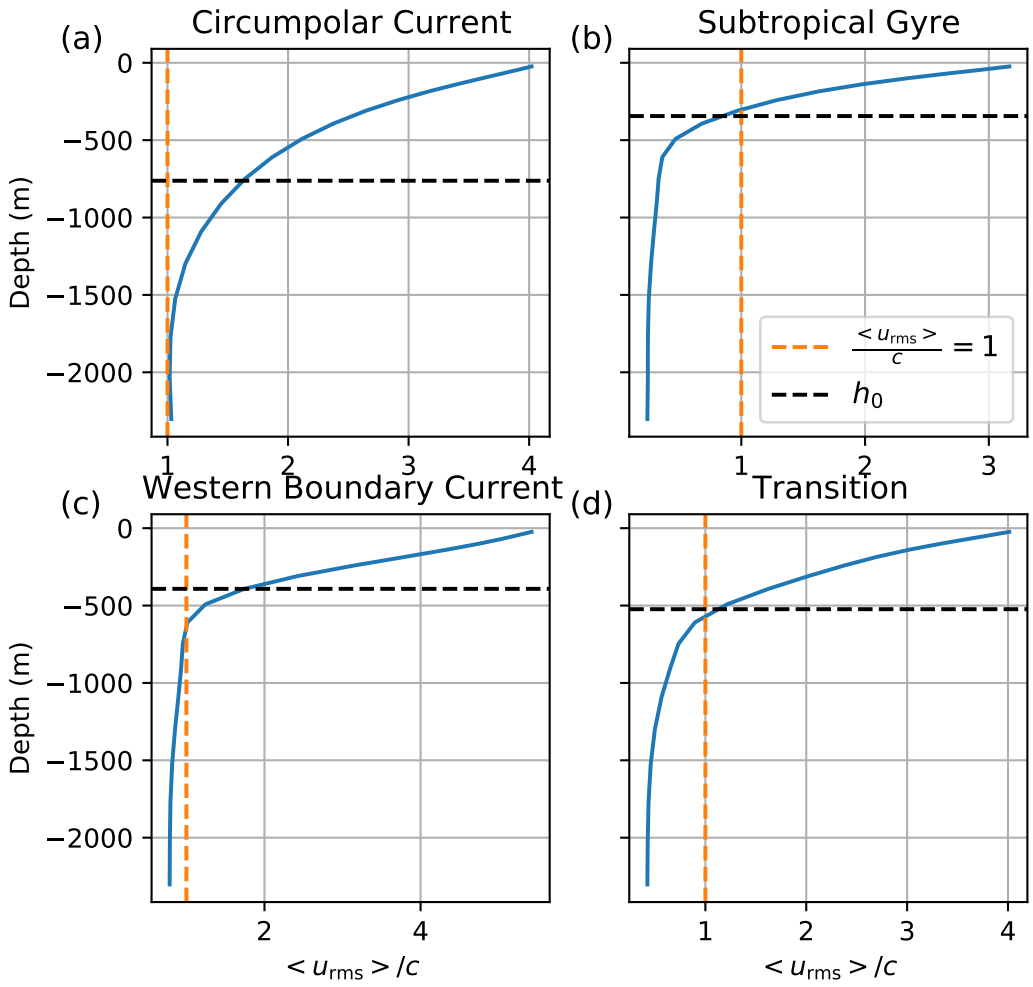

Figure 11. Vertical structure of the nonlinearity parameter (17) (blue line) in the four regions shown in figure 5. Orange dashed line is the nonlinearity parameter with value of 1. Black dashed line indicates the base of the thermocline, h_0.

rate, τ_0^{-1}, so

$$\gamma = \frac{u_{\rm rms}}{L_0} + \frac{1}{\tau_0}. \tag{19}$$

The eddy turnover rate, $u_{\rm rms}/L_0$, varies with depth and represents the contribution from nonlinear interactions (Ferrari & Nikurashin, 2010; Kong & Jansen, 2017). The decay time scale, τ_0, is depth-independent and associated with a superposition of linear waves. The form of γ in (19) is also found by Klocker et al. (2012), who point out that the decorrelation time scale is set by the turnover time of turbulent eddies in upper ocean and by the time scale of linear waves in deep ocean. Adopting (19) in (18), we obtain the composite formula

$$\kappa_{\rm comp} = \frac{u_{rms} L_0}{1 + L_0/(u_{\rm rms}\tau_0)}. \tag{20}$$

The advantage of (20) is that it can smoothly transition between the Prandtl and Taylor regimes. If $u_{\rm rms}/L_0$ dominates over τ_0^{-1}, (20) will reduce to the Prandtl regime expression, while if τ_0^{-1} dominates, (20) reduces to the Taylor regime expression. Since $u_{\rm rms}$ decays rapidly with depth, the mixing regime described by (20) transitions from the Prandtl regime to the Taylor regime with depth.

In Ferrari and Nikurashin (2010)'s derivation, the inverse of the decorrelation rate, $1/\gamma$, is equal to the time scale, τ, in the suppression factor (11). However, if $\tau = (u_{rms}/L_0 + 1/\tau_0)^{-1}$ is used in (11), the relation $\kappa_2 \approx \kappa_1 {\rm F}_s$ no longer holds (not shown)—it is therefore better to treat τ as a depth-independent time scale (i.e., $\tau = \tau_0$). This mismatch between τ and $1/\gamma$ is was also noted by Klocker and Abernathey (2014), who attributed it to a shortcoming of the stochastic models of Ferrari and Nikurashin (2010) and Klocker et al. (2012). The fits of κ_2 to $\kappa_1 {\rm F}_s$ in the circumpolar current, subtropical gyre and transition regions (c.f. section 4.1 and figure 8) gives τ_0 as 19 days, 25 days and 33 days, respectively, assuming the length scale, L, in (11) is given by the local energy-containing scale, L_0. The fit in the western boundary current is not reliable because κ_2 contains many negative values at that location. The time scales from the fits are close to the spin-down time scale due to the model's linear bottom drag, 25 days, which suggests τ_0 is related to frictional processes. We have no quantitative explanation for the spatial variation of τ_0, so for simplicity we choose it to be a uniform constant. Following Groeskamp et al. (2020), we estimate it by doing an overall fit using diffusivity profiles from all three regions and find $\tau_0 \approx 23$ days—which is again close to the frictional spin-down time.

The composite scaling, $\kappa_{\rm comp}$, with $\tau_0 = 23$ days is compared to the vertical structure of the major diffusivity, κ_1, in figure 9 (red dashed line). The composite scaling captures the variation of full-depth diffusivity better than MLT (purple dashed line) in the three basin regions. In the circumpolar current, the composite scaling slightly underestimates the diffusivity compared with MLT, but the overall comparison with κ_1 is still satisfactory. The success of the composite theory verifies our assumption that both the nonlinear eddy-eddy interaction and decay of linear waves contribute to the mixing. By accounting for both processes, the composite scaling can achieve a smooth transition between the nonlinear and linear regimes, which is promising to be applied to broad ocean scenarios.

The cross-stream diffusivity, κ_2, is also estimated by multiplying $\kappa_{\rm comp}$ by the suppression factor ${\rm F}_s^0$,

$${\rm F}_{\rm s}^0 = \frac{1}{1 + [\frac{\tau_0}{L_0}(c_w - \bar{u})]^2}, \tag{21}$$

where c_w and $\bar{u}$ are taken the same as those in section 4.1. The estimate of $\kappa_{\rm comp}{\rm F}_s^0$ is shown by the red dashed line in figure 8. The estimate with SMLT (i.e., $u_{\rm rms} L_0 {\rm F}_s^0$) is also plotted in figure 8 (green dashed line) for comparison. SMLT only captures the vertical structure of κ_2 well in the circumpolar current region, while the suppressed composite scaling, $\kappa_{\rm comp}{\rm F}_s^0$, works well in both the circumpolar current and gyres. The inaccurate estimate in the western boundary current might be due to the presence of neg-

ative values for the minor diffusivity (figure 3), which could potentially lead to large uncertainties for the scaling. The suppressed composite scaling is applicable to broader ocean regimes than SMLT, which makes it a promising estimate for the cross-stream diffusivity from ocean observations.

5 Conclusions

This study investigates the vertical structure of the isopycnal tracer diffusivity in an idealized basin configuration of MITgcm, which contains multiple gyres, boundary currents, and a zonally reentrant channel flow analogous to the Antarctic Circumpolar Current. Multiple tracers are advected to solve for the 3D diffusivity tensor based on a tracer-inversion method of S. D. Bachman et al. (2015). The isopycnal tracer diffusivity is well-characterized by the first two eigenvalues of the symmetric part of the diffusivity tensor, which are dominantly oriented along and across the mean flow, respectively. The isopycnal mixing is anisotropic with the diffusivity along the mean flow generally several times larger than the diffusivity across the mean flow. The cross-stream diffusivity tends to have a subsurface maximum, which can be reconstructed using the vertical profile of along-stream diffusivity after considering the suppression of mixing by the eddy propagation relative to the mean flow (K. S. Smith & Marshall, 2009; Ferrari & Nikurashin, 2010; Klocker et al., 2012). This suggests that the anisotropy of mixing is primarily due to the mean flow suppression of the cross-stream mixing. The signature of shear dispersion is not detected in the along-stream diffusivity, and the reason is still unclear to us.

The vertical structure of the along-stream diffusivity is well captured by the Prandtl mixing length theory with a depth-independent mixing length in the circumpolar current and above the thermocline in the basin regions. The mixing length is well-approximated by the energy containing scale estimated from the peak of the surface energy spectrum, which echos the theory of Larichev and Held (1995). Thompson and Young (2006) casts doubt on the assumption of energy containing scale as the mixing length in a two-mode quasigeostrophic turbulence dominated by coherent vortices. However, they estimated the energy containing scale from the barotropic streamfunction, while we estimate it from the SSH spectrum. The SSH spectrum is more reflective of the baroclinic modes than the barotropic mode (Wunsch, 1997), so Thompson and Young (2006)'s dissent does not necessarily apply to our estimate of mixing length. The mixing length in the ocean can thus be estimated as the energy-containing scale from the local surface energy spectrum, which is straightforward to diagnose from SSH observations from satellite altimetry (Scott & Wang, 2005; Le Traon et al., 2008; Zhou et al., 2015). No nondimensional mixing efficiency needs to be specified in this scaling, which is an advantage over previous studies (e.g., Klocker & Abernathey, 2014; Groeskamp et al., 2020). The energy containing scale is larger than the forcing scale because of the inverse energy cascade driven by nonlinear eddy-eddy interactions (Rhines, 1979; Larichev & Held, 1995), which is consistent with the observation that mixing in the upper extratropical ocean is controlled by the nonlinear edddies (Klocker & Abernathey, 2014; R. Abernathey & Wortham, 2015). The success of Prandtl scaling in the upper ocean provides a rationalization for studies which apply mixing length theory to infer the vertical structure of diffusivity, assuming that the mixing length is depth-independent (Bates et al., 2014; Groeskamp et al., 2020).

A depth-independent mixing length does not apply to the diffusivity below the thermocline in the basin. Indeed, using the upper-ocean mixing length can overestimate the deep diffusivity in the gyres by nearly an order of magnitude. Although the diffusivity is generally small at depth, excessively large diffusivities may still significantly impact deep watermasses and the mean state over long simulations since the mean flow is also very weak at depth. It is therefore important to develop a better scaling for the deep diffusivity in the basin. We find that below the thermocline in the basin, the along-stream diffusivity is well captured by the Taylor regime (i.e., a depth-independent mixing time scale times the EKE). The mixing time scale is close to the spin-down time scale due to

the model's linear bottom drag, indicating that the mixing might be controlled by bottom friction in deep ocean. The mixing regime transition with depth in the basin is related to the transition from a nonlinear to a linear regime across the thermocline, shown by the vertical profile of the nonlinearity parameter. This suggests that the Prandtl and Taylor regimes describe mixing due to nonlinear and linear processes, respectively. This is consistent with the arguments of Klocker and Abernathey (2014) and Klocker et al. (2016), who find that mixing length theory applies to surface mixing in the extratropics where the flow is nonlinear but fails in the tropics where the flow is dominated by linear waves. This study further suggests that this mixing regime transition also occurs in the vertical with a critical depth approximated by the base of thermocline in the midlatitude ocean.

Mixing length theory only characterizes the *full-depth* diffusivity well in the circumpolar current, because it assumes that the decorrelation rate of the mixing is set by the turnover rate of nonlinear eddies, while linear waves dominate in deep ocean in the basin. To account for the contribution of mixing by both nonlinear and linear processes, this study derives a composite scaling theory in which the decorrelation rate has contributions from both the eddy turnover rate and a depth-independent decay rate. This theory reduces to the Prandtl mixing length theory when the eddy turnover rate dominates and reduces to the Taylor regime when the frictional decay rate dominates. As the eddy kinetic energy decreases with depth, the composite scaling can smoothly transition from the Prandtl to Taylor regime. The composite scaling captures the vertical structure of the along-stream diffusivity better than the Prandtl mixing length theory, which suggests that both the nonlinear and linear processes play a role in the mixing. The cross-stream diffusivity is also well-characterized by the composite scaling multiplied by a suppression factor, (11), which accounts for the suppression of mixing by the mean flow (Ferrari & Nikurashin, 2010; Klocker et al., 2012). The composite scaling theory of this study has the advantage of a smooth transition between the nonlinear and linear regimes and should be useful in estimates or parameterizations of the full-depth isopycnal mixing in a broad range of ocean regimes.

The scaling proposed by this study is not a full closure theory, because it still requires the vertical profile of the eddy kinetic energy and the energy containing scale from the surface energy spectrum. Tests of the existing closure theories for the mixing length (e.g., Visbeck et al., 1997; Eden & Greatbatch, 2008; Thompson & Young, 2006; Jansen et al., 2015; Gallet & Ferrari, 2020, 2021) and vertical mode theory of the eddy kinetic energy (e.g., Wunsch, 1997; Lapeyre & Klein, 2006; LaCasce & Mahadevan, 2006; K. S. Smith & Vanneste, 2013; Lacasce, 2017; Groeskamp et al., 2020) is out of the scope of this study and will be studied in a forthcoming paper. In addition, the mean flow suppression theory used in this study is based on a single energy containing wavenumber as in Ferrari and Nikurashin (2010). However, studies have suggested that better estimate of the diffusivity can be gotten by calculating with the whole energy spectrum (Chen et al., 2015; Kong & Jansen, 2017). Thus for a full closure, we might also need a prediction theory for the EKE spectrum. A closure theory including all these factors would serve as a solid parameterization of the isopycnal mixing in the ocean component of coarse-resolution climate models.

Appendix A Goodness of fit for the diffusivity scalings

The goodness of fit for the scaling of both the major and minor diffusivities is measured by the fraction of variance unexplained (FVU),

$$\mathrm{FVU} = \frac{\int_{-H}^{0}(\kappa_{\mathrm{obs}} - \kappa_{fit})^2 dz}{\int_{-H}^{0}(\kappa_{\mathrm{obs}} - \bar{\kappa}^z_{\mathrm{obs}})^2 dz}, \tag{A1}$$

where κ_{obs} is the diagnosed diffusivity, κ^z_{obs} is the vertical average of κ_{obs}, and κ_{fit} is the fit of the scaling theory to κ_{obs}. Smaller FVU indicates better fitting. If FVU is larger

than one, that means κ_{fit} explains less of the vertical variation of κ_{obs} than the mean of κ_{obs}.

The FVU for the fits of the vertical profile of the major diffusivity, κ_1, and minor diffusivity, κ_2, is calculated at each grid point. Figure A1 shows the distribution of the FVU for the fit of κ_1 above and below the thermocline depth, h_0, to the Prandtl scaling (13) and Taylor scaling (16), respectively. The FVU for the fit of (13) is smaller than 0.5 in most of the extratropics. Large values are found along the western and southern boundaries and in the western boundary current extension, which might be related to the eddy decay due to the lateral friction at the boundary and the upgradient flux that drives the recirculation gyres downstream of the western boundary current (Waterman & Jayne, 2010; Chen & Waterman, 2017). Prandtl scaling is not effective in the tropics (figure A1a), where mixing is dominated by wave dynamics (Klocker et al., 2016). In section 4.3 we find that mixing below the thermocline is also dominated by wave dynamics and is better characterized by the Taylor scaling. The excellent fit with Taylor scaling in both the tropics and gyres shown in figure A1b supports our argument that the mixing dominated by wave dynamics is well-described by the Taylor scaling. The Taylor scaling does not fit κ_1 well in the channel because the vertical structure of κ_1 there follows the Prandtl scaling over full depth (figure 9a).

Figure A2 gives the distribution of the mixing length and time scales from the fits. The mixing length is typically tens of kilometers and decreases from low latitude to high latitude. The ratio of the mixing length to the local Rossby deformation radius increases from around 1 in the subtropics ($y \sim$ 1000–2000 km) to around 2.5 in the high latitude ($y \sim$ 4000 km), which is consistent with the observationally based results of Klocker and Abernathey (2014). The fitted mixing time scale is smallest in the tropics and appears uniform in the gyres, where it is close to the spin-down time scale due to the model's linear bottom drag, 25 days.

Figure A3 shows the distribution of the FVU for the minor diffusivity, κ_2, fit to the formula of $\kappa_1 \mathrm{F}_s$. Consistent with figure 8, $\kappa_1 \mathrm{F}_s$ fits κ_2 well in most of the extratropics, which suggests that the two diffusivities follow the same scaling. The misfits are larger in the western boundary currents, tropics, and southern part of the channel. The diffusivity takes on many negative values in these regions (figure 3) and the scaling theory cannot account for negative diffusivities.

Appendix B Identification and tracking of coherent mesoscale eddies

Coherent mesoscale eddies are identified and tracked from the SSH snapshots in three-day intervals from the model, using the same algorithm as Chelton et al. (2011). This method is provided as an optional tracking method in the eddy tracking package described by Mason et al. (2014). Coherent eddies are identified as the SSH extrema and tracked by connecting each eddy to the proximal eddies in successive successive time frames, where the eddies amplitude and radius are required to be 0.4–2.5 times those of the corresponding eddies in the last time frame. Only the eddies that last longer than 30 days are considered. The propagation velocity of coherent eddies at time step m is estimated as the centered difference from locations of the eddy centroids at the time steps $m-1$ and $m+1$. See Chelton et al. (2011) for more detail.

Acknowledgments

This work is supported by the National Science Foundation (NSF) through Award OCE-2048826. Computing resources were from the high-performance SeaWulf computing system provided by Stony Brook Research Computing and Cyber Infrastructure and the Institute for Advanced Computational Science at Stony Brook University, which is supported by NSF. We are grateful to Shafer Smith for insightful comments and sharing an

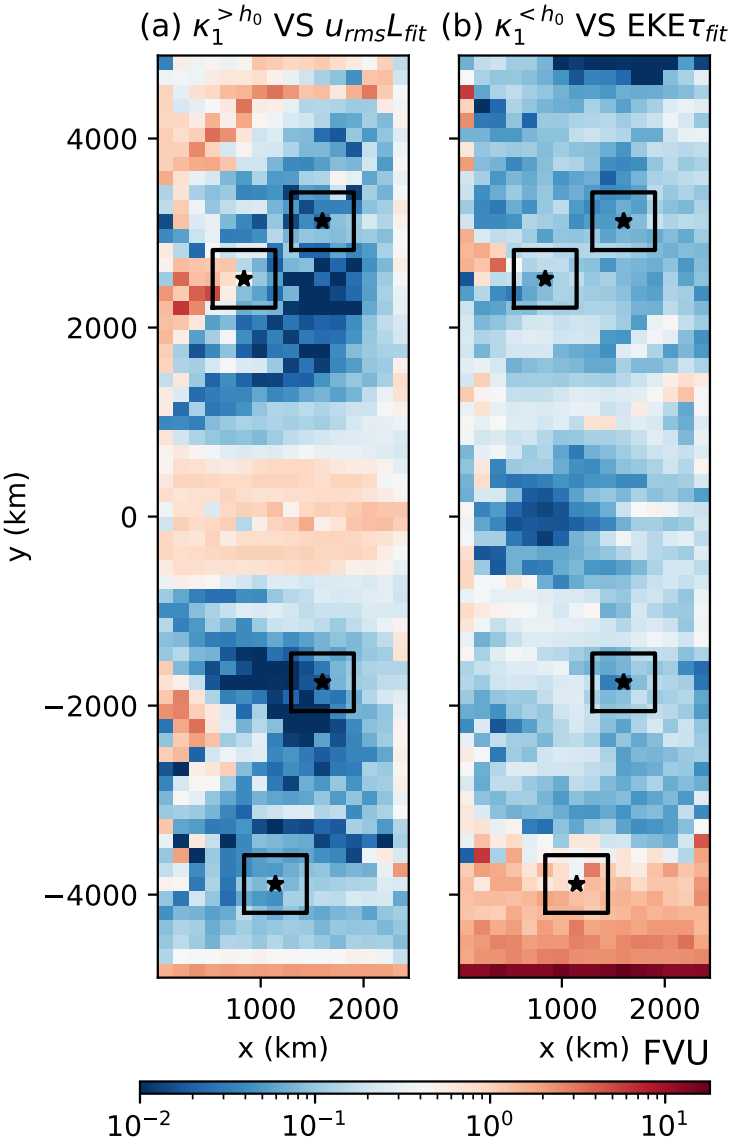

Figure A1. Fraction of variance unexplained (FVU) (A1) for the fits of the major diffusivity, κ_1, above and below the base of the thermocline, h_0, to (a) the Prandtl scaling (13) and (b) Taylor scaling (16), respectively. Black boxes are the regions where the vertical structures of the diffusivities are analyzed. Black stars indicate the locations where the scaling for the vertical structure of diffusivity is examined.

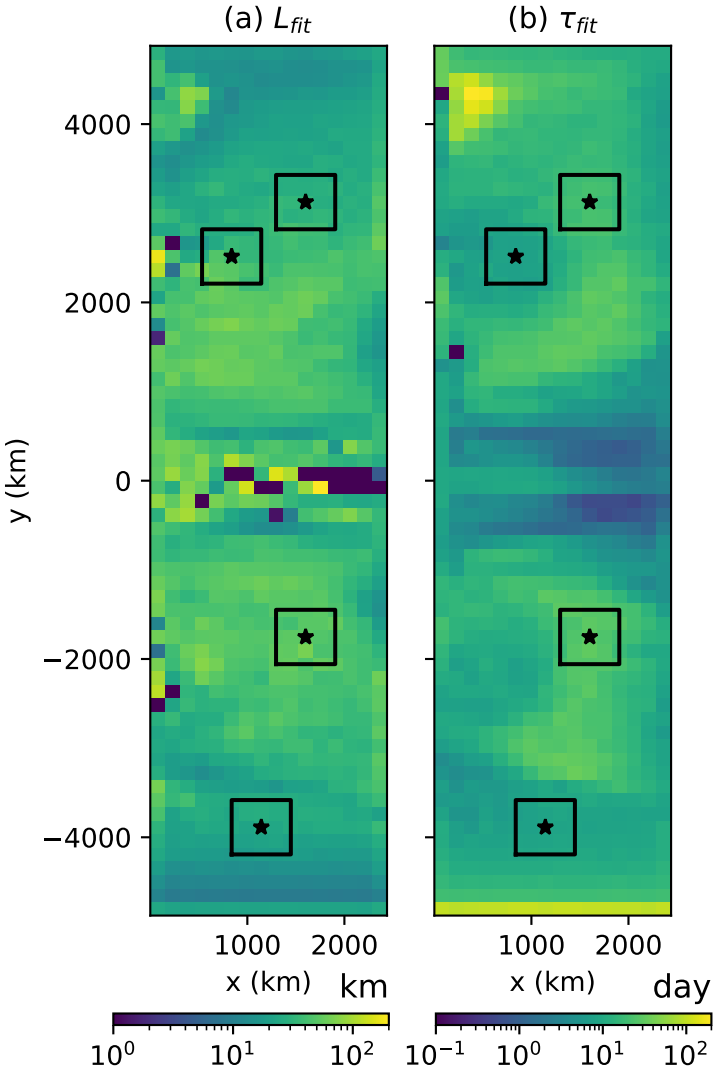

Figure A2. Distribution of the fitted mixing (a) length and (b) time scales in figure A1. The extreme values in (a) and (b) (grids with darkest color) are due to the presence of negative diffusivities at those points. Black boxes and stars are as in figure A1.

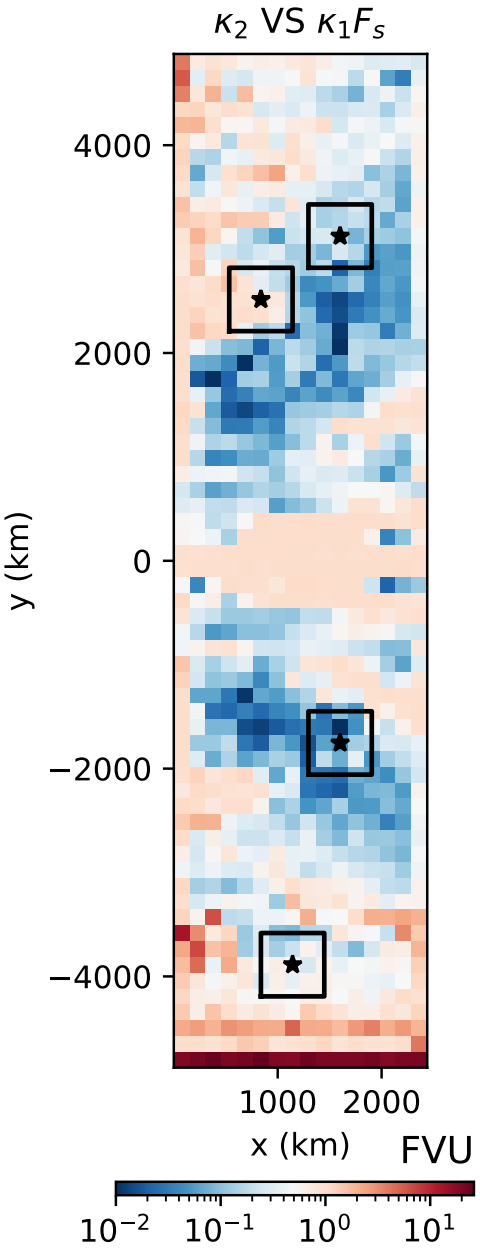

Figure A3. Fraction of variance unexplained (FVU) (A1) for the fits of the formula of $\kappa_1 \mathrm{F}_s$, with F_s given in (11), to the minor diffusivity, κ_2. Black boxes and stars are as in figure A1.

unpublished manuscript on the use of multiple tracers by Dhruv Balwada, Shafer Smith, and Ryan Abernathey. We also thank Scott Bachman and Yan Wang for helpful discussions on the tracer inversion method and analysis.

Model configuration, analysis scripts, data files used for this study are available at `https://drive.google.com/drive/folders/1ILzStZkWkrVwJyHovZuVlOMMZ2zcoUYF?usp=sharing`.

References

Abernathey, R., Ferreira, D., & Klocker, A. (2013). Diagnostics of isopycnal mixing in a circumpolar channel. *Ocean Modell.*, *72*, 1–16.

Abernathey, R., Marshall, J., Mazloff, M., & Shuckburgh, E. (2010). Enhancement of mesoscale eddy stirring at steering levels in the Southern Ocean. *Journal of Physical Oceanography*, *40*(1), 170–184.

Abernathey, R., & Wortham, C. (2015). Phase speed cross spectra of eddy heat fluxes in the eastern Pacific. *J. Phys. Oceanogr.*, *45*(5), 1285–1301.

Abernathey, R. P., & Marshall, J. (2013). Global surface eddy diffusivities derived from satellite altimetry. *J. Geophys. Res. Oceans*, *118*(2), 901–916.

Bachman, S., & Fox-Kemper, B. (2013). Eddy parameterization challenge suite I: Eady spindown. *Ocean Modell.*, *64*, 12–28.

Bachman, S. D., Fox-Kemper, B., & Bryan, F. O. (2015). A tracer-based inversion method for diagnosing eddy-induced diffusivity and advection. *Ocean Modell.*, *86*, 1–14.

Bachman, S. D., Fox-Kemper, B., & Bryan, F. O. (2020). A diagnosis of anisotropic eddy diffusion from a high-resolution global ocean model. *J. Adv. Model. Earth Sys.*, *12*(2), e2019MS001904.

Balwada, D., Speer, K. G., LaCasce, J. H., Owens, W. B., Marshall, J., & Ferrari, R. (2016). Circulation and stirring in the Southeast Pacific Ocean and the Scotia Sea sectors of the Antarctic Circumpolar Current. *J. Phys. Oceanogr.*, *46*(7), 2005–2027.

Bates, M., Tulloch, R., Marshall, J., & Ferrari, R. (2014). Rationalizing the spatial distribution of mesoscale eddy diffusivity in terms of mixing length theory. *J. Phys. Oceanogr.*, *44*(6), 1523–1540.

Campin, J.-M., Heimbach, P., Losch, M., Forget, G., Hill, E., Adcroft, A., ... Dussin, R. (2020). *MITgcm.* Zenodo. doi: 10.5281/zenodo.3967889

Cessi, P. (2008). An energy-constrained parameterization of eddy buoyancy flux. *J. Phys. Oceanogr.*, *38*(8), 1807–1819.

Cessi, P., & Wolfe, C. L. (2009). Eddy-driven buoyancy gradients on eastern boundaries and their role in the thermocline. *J. Phys. Oceanogr.*, *39*(7), 1595–1614.

Cessi, P., Wolfe, C. L., & Ludka, B. C. (2010). Eastern-boundary contribution to the Residual and Meridional Overturning Circulations. *J. Phys. Oceanogr.*, *40*(9), 2075–2090. doi: 10.1175/2010JPO4426.1

Chapman, C., & Sallée, J.-B. (2017). Isopycnal mixing suppression by the Antarctic Circumpolar Current and the Southern Ocean meridional overturning circulation. *Journal of Physical Oceanography*, *47*(8), 2023–2045.

Chelton, D. B., Schlax, M. G., & Samelson, R. M. (2011). Global observations of nonlinear mesoscale eddies. *Prog. Oceanogr.*, *91*(2), 167–216.

Chelton, D. B., Schlax, M. G., Samelson, R. M., & de Szoeke, R. A. (2007). Global observations of large oceanic eddies. *Geophys. Res. Lett.*, *34*(15).

Chen, R., Gille, S. T., McClean, J. L., Flierl, G. R., & Griesel, A. (2015). A multi-wavenumber theory for eddy diffusivities and its application to the southeast Pacific (DIMES) region. *Journal of Physical Oceanography*, *45*(7), 1877–1896.

Chen, R., McClean, J. L., Gille, S. T., & Griesel, A. (2014). Isopycnal eddy diffusivities and critical layers in the Kuroshio Extension from an eddying ocean

model. *Journal of physical oceanography*, *44*(8), 2191–2211.

Chen, R., & Waterman, S. (2017). Mixing nonlocality and mixing anisotropy in an idealized western boundary current jet. *J. Phys. Oceanogr.*, *47*(12), 3015–3036.

Cole, S. T., Wortham, C., Kunze, E., & Owens, W. B. (2015). Eddy stirring and horizontal diffusivity from Argo float observations: Geographic and depth variability. *Geophys. Res. Lett.*, *42*(10), 3989–3997.

Daru, V., & Tenaud, C. (2004). High order one-step monotonicity-preserving schemes for unsteady compressible flow calculations. *Journal of computational physics*, *193*(2), 563–594.

Eden, C., & Greatbatch, R. J. (2008). Towards a mesoscale eddy closure. *Ocean Modell.*, *20*(3), 223–239.

Ferrari, R., & Nikurashin, M. (2010). Suppression of eddy diffusivity across jets in the Southern Ocean. *J. Phys. Oceanogr.*, *40*(7), 1501–1519.

Ferrari, R., & Wunsch, C. (2009). Ocean circulation kinetic energy: Reservoirs, sources, and sinks. *Annu. Rev. Fluid Mech.*, *41*, 253–282.

Fox-Kemper, B., Lumpkin, R., & Bryan, F. (2013). Lateral transport in the ocean interior. In G. Siedler, S. M. Griffies, J. Gould, & J. A. Church (Eds.), *Ocean circulation and climate* (Vol. 103, pp. 185–209). Academic Press. doi: 10.1016/B978-0-12-391851-2.00008-8

Gallet, B., & Ferrari, R. (2020). The vortex gas scaling regime of baroclinic turbulence. *Proc. Natl. Acad. Sci. USA*, *117*(9), 4491–4497.

Gallet, B., & Ferrari, R. (2021). A quantitative scaling theory for meridional heat transport in planetary atmospheres and oceans. *AGU Advances*, *2*(3), e2020AV000362.

Gent, P. R., & Mcwilliams, J. C. (1990). Isopycnal mixing in ocean circulation models. *J. Phys. Oceanogr.*, *20*(1), 150–155.

Gent, P. R., Willebrand, J., McDougall, T. J., & McWilliams, J. C. (1995). Parameterizing eddy-induced tracer transports in ocean circulation models. *J. Phys. Oceanogr.*, *25*(4), 463–474.

Gnanadesikan, A., Pradal, M.-A., & Abernathey, R. (2015). Isopycnal mixing by mesoscale eddies significantly impacts oceanic anthropogenic carbon uptake. *Geophys. Res. Lett.*, *42*(11), 4249–4255.

Green, J. (1970). Transfer properties of the large-scale eddies and the general circulation of the atmosphere. *Q. J. R. Met. Soc.*, *96*(408), 157–185.

Griesel, A., Eden, C., Koopmann, N., & Yulaeva, E. (2015). Comparing isopycnal eddy diffusivities in the Southern Ocean with predictions from linear theory. *Ocean Modell.*, *94*, 33–45.

Griesel, A., McClean, J., Gille, S., Sprintall, J., & Eden, C. (2014). Eulerian and Lagrangian isopycnal eddy diffusivities in the Southern Ocean of an eddying model. *J. Phys. Oceanogr.*, *44*(2), 644–661.

Griffies, S. M. (1998). The gent–mcwilliams skew flux. *J. Phys. Oceanogr.*, *28*(5), 831–841.

Groeskamp, S., LaCasce, J. H., McDougall, T. J., & Rogé, M. (2020). Full-depth global estimates of ocean mesoscale eddy mixing from observations and theory. *Geophysical Research Letters*, e2020GL089425.

Groeskamp, S., Sloyan, B. M., Zika, J. D., & McDougall, T. J. (2017). Mixing inferred from an ocean climatology and surface fluxes. *J. Phys. Oceanogr.*, *47*(3), 667–687.

Haidvogel, D. B., & Held, I. M. (1980). Homogeneous quasi-geostrophic turbulence driven by a uniform temperature gradient. *J. Atmos. Sci.*, *37*(12), 2644–2660.

Hallberg, R., & Gnanadesikan, A. (2006). The role of eddies in determining the structure and response of the wind-driven Southern Hemisphere overturning: Results from the modeling eddies in the Southern Ocean (MESO) project. *J. Phys. Oceanogr.*, *36*(12), 2232–2252.

Held, I. M., & Larichev, V. D. (1996). A scaling theory for horizontally homogeneous, baroclinically unstable flow on a beta plane. *J. Atmos. Sci.*, *53*(7), 946–952.

Jansen, M. F., Adcroft, A. J., Hallberg, R., & Held, I. M. (2015). Parameterization of eddy fluxes based on a mesoscale energy budget. *Ocean Modell.*, *92*, 28–41.

Jones, C., & Abernathey, R. P. (2019). Isopycnal mixing controls deep ocean ventilation. *Geophysical Research Letters*, *46*(22), 13144–13151.

Kamenkovich, I., Rypina, I. I., & Berloff, P. (2015). Properties and origins of the anisotropic eddy-induced transport in the North Atlantic. *Journal of Physical Oceanography*, *45*(3), 778–791.

Killworth, P. D. (1997). On the parameterization of eddy transfer Part I. Theory. *Journal of Marine Research*, *55*(6), 1171–1197.

Klocker, A., & Abernathey, R. (2014). Global patterns of mesoscale eddy properties and diffusivities. *J. Phys. Oceanogr.*, *44*(3), 1030–1046.

Klocker, A., Ferrari, R., & LaCasce, J. H. (2012). Estimating suppression of eddy mixing by mean flows. *J. Phys. Oceanogr.*, *42*(9), 1566–1576.

Klocker, A., & Marshall, D. P. (2014). Advection of baroclinic eddies by depth mean flow. *Geophys. Res. Lett.*, *41*(10), 3517–3521.

Klocker, A., Marshall, D. P., Keating, S. R., & Read, P. L. (2016). A regime diagram for ocean geostrophic turbulence. *Q. J. R. Met. Soc.*, *142*(699), 2411–2417.

Kong, H., & Jansen, M. (2017). The eddy diffusivity in barotropic β-plane turbulence. *Fluids*, *2*(4), 54.

Lacasce, J. H. (2017). The prevalence of oceanic surface modes. *Geophysical Research Letters*, *44*(21), 11–097.

LaCasce, J. H., & Mahadevan, A. (2006). Estimating subsurface horizontal and vertical velocities from sea-surface temperature. *Journal of Marine Research*, *64*(5), 695–721.

Lapeyre, G., & Klein, P. (2006). Dynamics of the upper oceanic layers in terms of surface quasigeostrophy theory. *Journal of physical oceanography*, *36*(2), 165–176.

Larichev, V. D., & Held, I. M. (1995). Eddy amplitudes and fluxes in a homogeneous model of fully developed baroclinic instability. *J. Phys. Oceanogr.*, *25*(10), 2285–2297.

Ledwell, J. R., Watson, A. J., & Law, C. S. (1998). Mixing of a tracer in the pycnocline. *Journal of Geophysical Research: Oceans*, *103*(C10), 21499–21529.

Le Traon, P.-Y., Klein, P., Hua, B. L., & Dibarboure, G. (2008). Do altimeter wavenumber spectra agree with the interior or surface quasigeostrophic theory? *Journal of Physical Oceanography*, *38*(5), 1137–1142.

Marshall, D. P., & Adcroft, A. J. (2010). Parameterization of ocean eddies: Potential vorticity mixing, energetics and arnold?s first stability theorem. *Ocean Modell.*, *32*(3-4), 188–204.

Marshall, D. P., Maddison, J. R., & Berloff, P. S. (2012). A framework for parameterizing eddy potential vorticity fluxes. *J. Phys. Oceanogr.*, *42*(4), 539–557.

Marshall, J., Adcroft, A., Hill, C., Perelman, L., & Heisey, C. (1997). A finite-volume, incompressible Navier Stokes model for studies of the ocean on parallel computers. *J. Geophys. Res.*, *102*(C3), 5753-5766. doi: 10.1029/96JC02775

Marshall, J., Hill, C., Perelman, L., & Adcroft, A. (1997). Hydrostatic, quasi-hydrostatic, and nonhydrostatic ocean modeling. *J. Geophys. Res.*, *102*(C3), 5733-5752. doi: 10.1029/96JC02776

Marshall, J., & Radko, T. (2003). Residual-mean solutions for the Antarctic Circumpolar Current and its associated overturning circulation. *J. Phys. Oceanogr.*, *33*(11), 2341–2354.

Marshall, J., & Radko, T. (2006). A model of the upper branch of the meridional overturning of the Southern Ocean. *Prog. Oceanogr.*, *70*(2-4), 331–345.

Marshall, J., Scott, J. R., Romanou, A., Kelley, M., & Leboissetier, A. (2017). The dependence of the oceans MOC on mesoscale eddy diffusivities: A model study. *Ocean Modell.*, *111*, 1–8.

Marshall, J., Shuckburgh, E., Jones, H., & Hill, C. (2006). Estimates and implications of surface eddy diffusivity in the Southern Ocean derived from tracer transport. *J. Phys. Oceanogr.*, *36*(9), 1806–1821.

Mason, E., Pascual, A., & McWilliams, J. C. (2014). A new sea surface height–based code for oceanic mesoscale eddy tracking. *J. Atmos. Oceanic Technol.*, *31*(5), 1181–1188.

McGillicuddy Jr, D., Anderson, L., Doney, S., & Maltrud, M. (2003). Eddy-driven sources and sinks of nutrients in the upper ocean: Results from a 0.1° resolution model of the North Atlantic. *Global Biogeochem. Cy.*, *17*(2).

Moore, E. H. (1920). On the reciprocal of the general algebraic matrix. *Bull. Am. Math. Soc.*, *26*, 394–395.

Pennel, R., & Kamenkovich, I. (2014). On the factors controlling the eddy-induced transport in the Antarctic Circumpolar Current. *Journal of physical oceanography*, *44*(8), 2127–2138.

Penrose, R. (1955). A generalized inverse for matrices. *Math. Proc. Cambridge*, *51*(3), 406–413.

Prandtl, L. (1925). Bericht über Untersuchungen zur ausgebildeten Turbulenz. *ZAMM-Z. Angew. Math. Me.*, *5*(2), 136–139.

Redi, M. H. (1982). Oceanic isopycnal mixing by coordinate rotation. *J. Phys. Oceanogr.*, *12*(10), 1154–1158.

Rhines, P. B. (1979). Geostrophic turbulence. *Annu. Rev. Fluid Mech.*, *11*(1), 401–441.

Riha, S., & Eden, C. (2011). Lagrangian and Eulerian lateral diffusivities in zonal jets. *Ocean Modell.*, *39*(1-2), 114–124.

Roach, C. J., Balwada, D., & Speer, K. (2018). Global observations of horizontal mixing from Argo float and surface drifter trajectories. *J. Geophys. Res. Oceans*, *123*(7), 4560–4575.

Rypina, I. I., Kamenkovich, I., Berloff, P., & Pratt, L. J. (2012). Eddy-induced particle dispersion in the near-surface North Atlantic. *J. Phys. Oceanogr.*, *42*(12), 2206–2228. doi: 10.1175/jpo-d-11-0191.1

Scott, R. B., & Wang, F. (2005). Direct evidence of an oceanic inverse kinetic energy cascade from satellite altimetry. *J. Phys. Oceanogr.*, *35*(9), 1650–1666.

Siegenthaler, U. (1983). Uptake of excess CO_2 by an outcrop-diffusion model of the ocean. *J. Geophys. Res. Oceans*, *88*(C6), 3599–3608.

Smith, K. S. (2005). Tracer transport along and across coherent jets in two-dimensional turbulent flow. *J. Fluid Mech.*, *544*, 133–142.

Smith, K. S. (2007a). Eddy amplitudes in baroclinic turbulence driven by nonzonal mean flow: Shear dispersion of potential vorticity. *J. Phys. Oceanogr.*, *37*(4), 1037–1050.

Smith, K. S. (2007b). The geography of linear baroclinic instability in Earth's oceans. *J. Mar. Res.*, *65*(5), 655–683.

Smith, K. S., & Marshall, J. (2009). Evidence for enhanced eddy mixing at middepth in the Southern Ocean. *Journal of Physical Oceanography*, *39*(1), 50–69.

Smith, K. S., & Vanneste, J. (2013). A surface-aware projection basis for quasi-geostrophic flow. *Journal of physical oceanography*, *43*(3), 548–562.

Smith, R. D., & Gent, P. R. (2004). Anisotropic Gent–McWilliams parameterization for ocean models. *Journal of Physical Oceanography*, *34*(11), 2541–2564.

Stammer, D. (1998). On eddy characteristics, eddy transports, and mean flow properties. *J. Phys. Oceanogr.*, *28*(4), 727–739.

Stanley, Z., Bachman, S., & Grooms, I. (2020). Vertical structure of ocean mesoscale eddies with implications for parameterizations of tracer transport. *Journal of*

Advances in Modeling Earth Systems, e2020MS002151.

Steinberg, J. M., Pelland, N. A., & Eriksen, C. C. (2019). Observed evolution of a California Undercurrent eddy. *J. Phys. Oceanogr.*, *49*(3), 649–674.

Taylor, G. I. (1922). Diffusion by continuous movements. *Proc. London Math.*, *2*(1), 196–212.

Taylor, G. I. (1953). Dispersion of soluble matter in solvent flowing slowly through a tube. *Proceedings of the Royal Society of London. Series A. Mathematical and Physical Sciences*, *219*(1137), 186–203.

Thompson, A. F., & Young, W. R. (2006). Scaling baroclinic eddy fluxes: Vortices and energy balance. *J. Phys. Oceanogr.*, *36*(4), 720–738.

Thompson, A. F., & Young, W. R. (2007). Two-layer baroclinic eddy heat fluxes: Zonal flows and energy balance. *J. Atmos. Sci.*, *64*(9), 3214–3231.

Tulloch, R., Ferrari, R., Jahn, O., Klocker, A., LaCasce, J., Ledwell, J. R., ... Watson, A. (2014). Direct estimate of lateral eddy diffusivity upstream of drake passage. *J. Phys. Oceanogr.*, *44*(10), 2593–2616. doi: 10.1175/jpo-d-13-0120.1

Tulloch, R., Marshall, J., Hill, C., & Smith, K. S. (2011). Scales, growth rates, and spectral fluxes of baroclinic instability in the ocean. *Journal of Physical Oceanography*, *41*(6), 1057–1076.

Tulloch, R., Marshall, J., & Smith, K. S. (2009). Interpretation of the propagation of surface altimetric observations in terms of planetary waves and geostrophic turbulence. *J. Geophys. Res. Oceans*, *114*(C2), 005. Retrieved from `http://dx.doi.org/10.1029/2008JC005055` doi: 10.1029/2008jc005055

Visbeck, M., Marshall, J., Haine, T., & Spall, M. (1997). Specification of eddy transfer coefficients in coarse-resolution ocean circulation models. *J. Phys. Oceanogr.*, *27*(3), 381–402.

Waterman, S., & Jayne, S. R. (2010). Eddy-mean flow interactions in the along-stream development of a western boundary current jet: An idealized model study. *J. Phys. Oceanogr.*.

Wei, H., & Wang, Y. (2021). Full-depth scalings for isopycnal eddy mixing across continental slopes under upwelling-favorable winds. *Journal of Advances in Modeling Earth Systems*, e2021MS002498.

Wolfe, C. L. (2014). Approximations to the ocean's residual circulation in arbitrary tracer coordinates. *Ocean Modell.*, *75*, 20–35. doi: 10.1016/j.ocemod.2013.12.004

Wolfe, C. L., & Cessi, P. (2009). Overturning circulation in an eddy-resolving model: The effect of the pole-to-pole temperature gradient. *J. Phys. Oceanogr.*, *39*(1), 125–142.

Wolfe, C. L., & Cessi, P. (2010). What sets the strength of the middepth stratification and overturning circulation in eddying ocean models? *J. Phys. Oceanogr.*, *40*(7), 1520–1538.

Wolfe, C. L., & Cessi, P. (2011). The adiabatic pole-to-pole overturning circulation. *J. Phys. Oceanogr.*, *41*(9), 1795–1810. doi: 10.1175/2011JPO4570.1

Wolfe, C. L., Cessi, P., McClean, J. L., & Maltrud, M. E. (2008). Vertical heat flux in eddying ocean models. *Geophys. Res. Lett.*, *35*, L23605. doi: 10.1029/2008GL036138

Wolfram, P. J., & Ringler, T. D. (2017). Quantifying residual, eddy, and mean flow effects on mixing in an idealized circumpolar current. *Journal of Physical Oceanography*, *47*(8), 1897–1920.

Wolfram, P. J., Ringler, T. D., Maltrud, M. E., Jacobsen, D. W., & Petersen, M. R. (2015). Diagnosing isopycnal diffusivity in an eddying, idealized midlatitude ocean basin via Lagrangian, in Situ, Global, High–Performance particle tracking (LIGHT). *J. Phys. Oceanogr.*, *45*(8), 2114–2133.

Wunsch, C. (1997). The vertical partition of oceanic horizontal kinetic energy. *Journal of Physical Oceanography*, *27*(8), 1770–1794.

Young, W., Rhines, P., & Garrett, C. (1982). Shear-flow dispersion, internal waves

and horizontal mixing in the ocean. *Journal of Physical Oceanography*, *12*(6), 515–527.

Zhou, X.-H., Wang, D.-P., & Chen, D. (2015). Global wavenumber spectrum with corrections for altimeter high-frequency noise. *Journal of Physical Oceanography*, *45*(2), 495–503.

Zhurbas, V., Lyzhkov, D., & Kuzmina, N. (2014). Drifter-derived estimates of lateral eddy diffusivity in the world ocean with emphasis on the Indian Ocean and problems of parameterisation. *Deep Sea Res. I*, *83*, 1–11.

Zhurbas, V., & Oh, I. S. (2003). Lateral diffusivity and lagrangian scales in the Pacific Ocean as derived from drifter data. *Journal of Geophysical Research: Oceans*, *108*(C5).

Zhurbas, V., & Oh, I. S. (2004). Drifter-derived maps of lateral diffusivity in the Pacific and Atlantic oceans in relation to surface circulation patterns. *J. Geophys. Res. Oceans*, *109*(C5).

Figure 1.

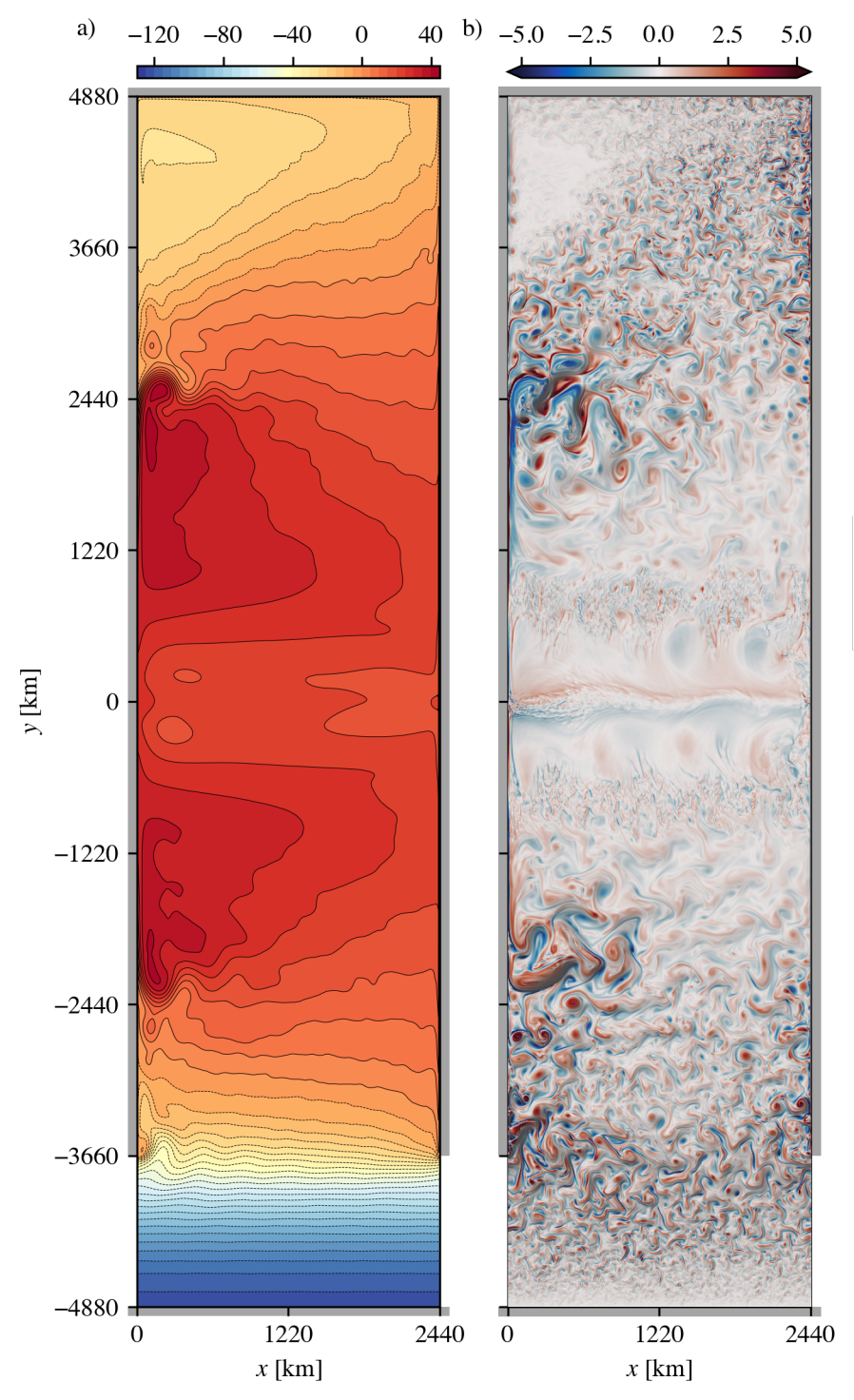
a)
−120
−80
−40
0
40
b)
−5.0
−2.5
0.0
2.5
5.0
4880
3660
2440
1220
0
−1220
−2440
−3660
−4880
y [km]
0
1220
2440
x [km]
0
1220
2440
x [km]

Figure 2.

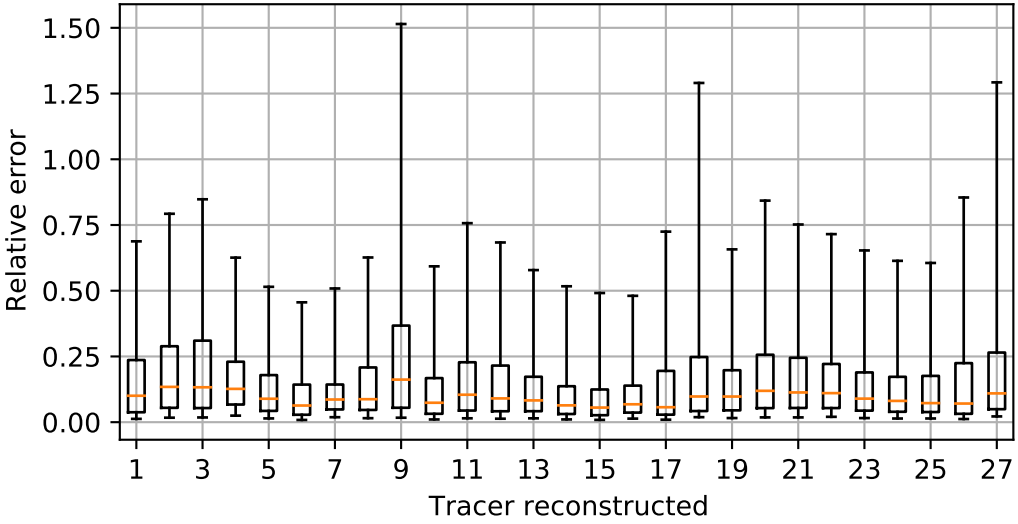
Relative error
1.50
1.25
1.00
0.75
0.50
0.25
0.00
1
3
5
7
9
11
13
15
17
19
21
23
25
27
Tracer reconstructed

Figure 3.

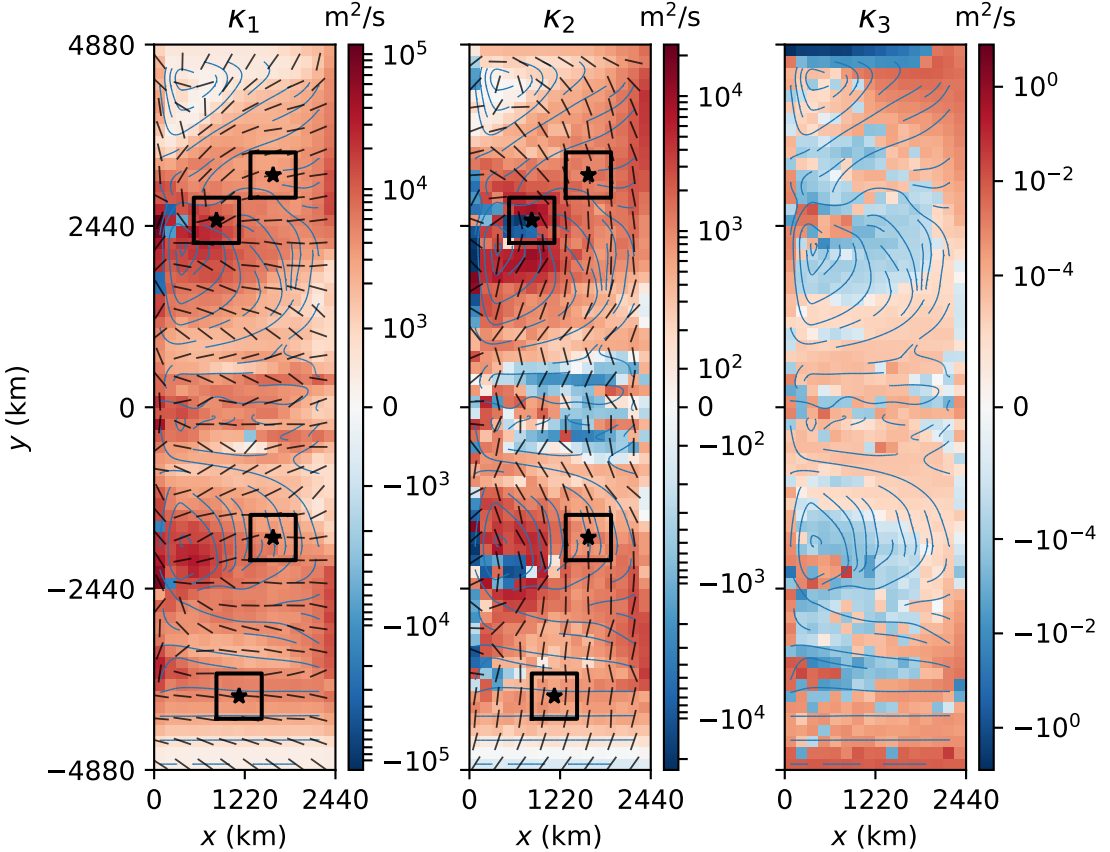
κ_1
m^2/s
κ_2
m^2/s
κ_3
m^2/s
4880
2440
0
−2440
−4880
y (km)
0
1220
2440
x (km)
10^5
10^4
10^3
0
-10^3
-10^4
-10^5
10^4
10^3
10^2
0
-10^2
-10^3
-10^4
10^0
10^{-2}
10^{-4}
0
-10^{-4}
-10^{-2}
-10^0

Figure 4.

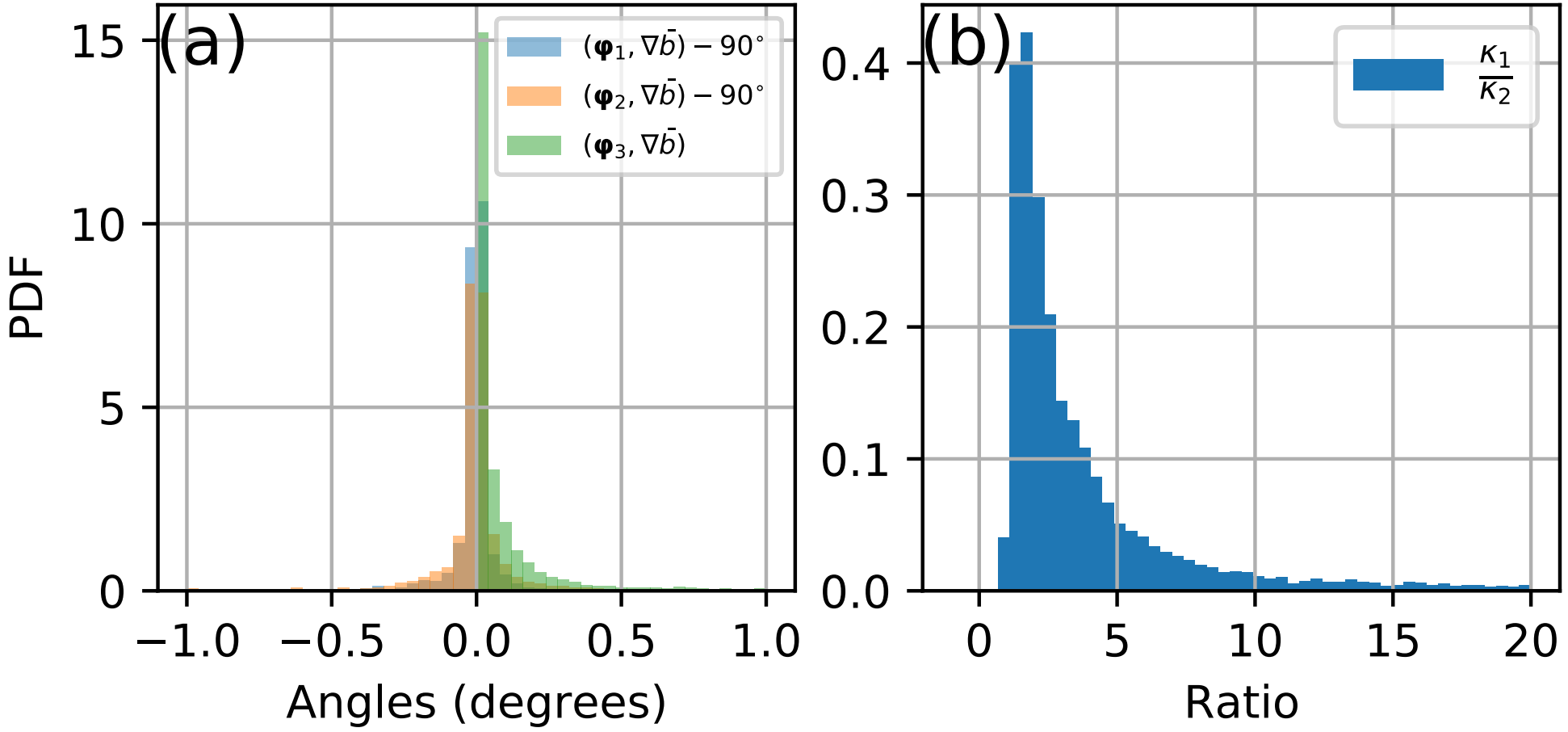
(a)
$(\boldsymbol{\varphi}_1, \nabla\bar{b}) - 90^\circ$
$(\boldsymbol{\varphi}_2, \nabla\bar{b}) - 90^\circ$
$(\boldsymbol{\varphi}_3, \nabla\bar{b})$
PDF
Angles (degrees)
(b)
$\frac{\kappa_1}{\kappa_2}$
Ratio

Figure 5.

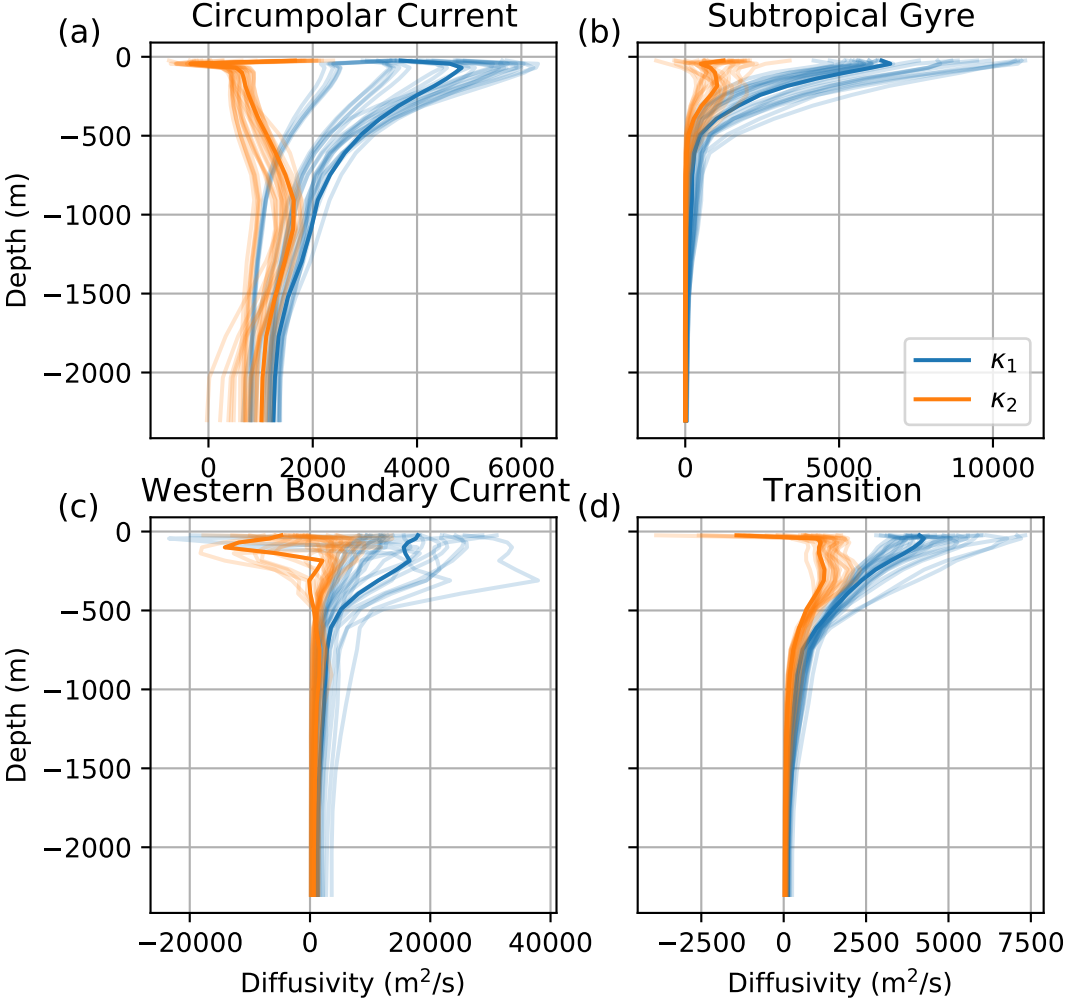
(a)
Circumpolar Current
(b)
Subtropical Gyre
(c)
Western Boundary Current
(d)
Transition
Depth (m)
0
−500
−1000
−1500
−2000
0
2000
4000
6000
0
5000
10000
−20000
0
20000
40000
−2500
0
2500
5000
7500
κ_1
κ_2
Diffusivity (m^2/s)
Diffusivity (m^2/s)

Figure 6.

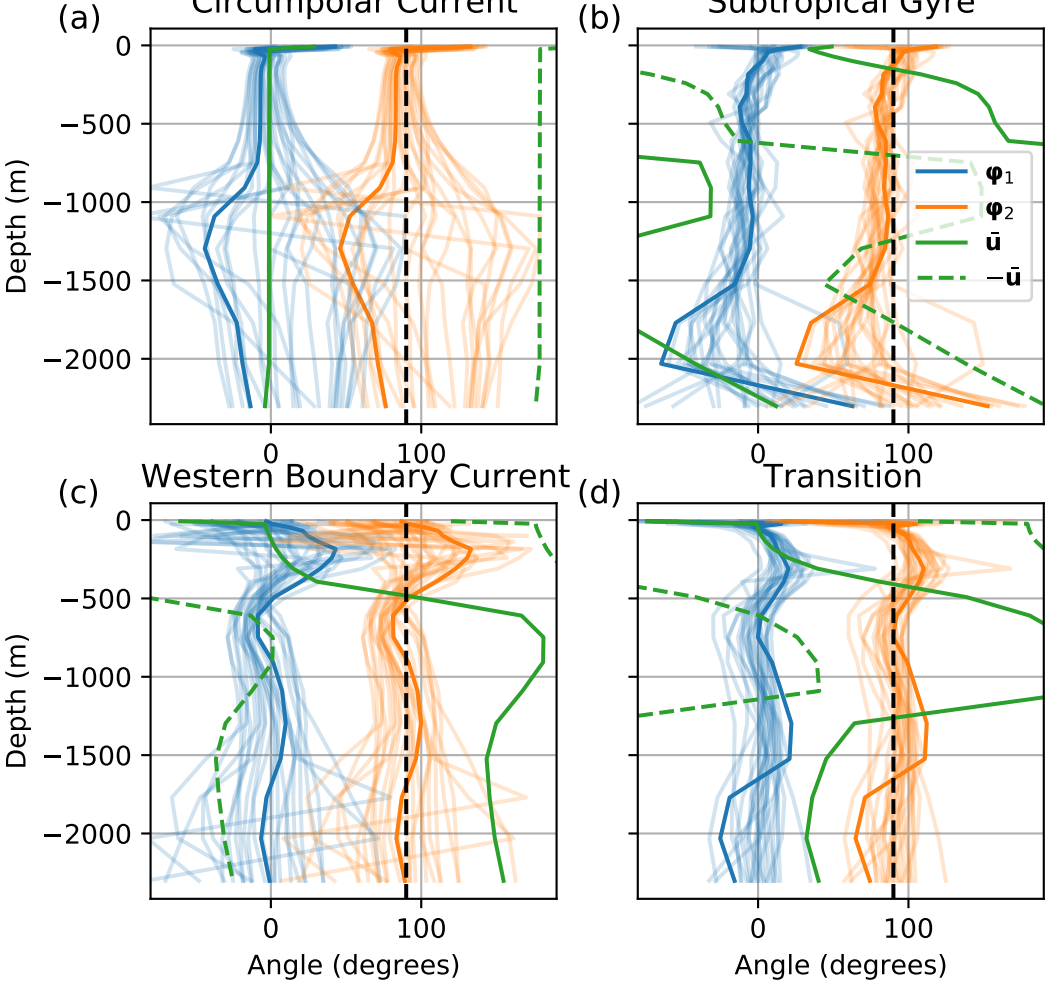
(a)
Circumpolar Current
(b)
Subtropical Gyre
(c)
Western Boundary Current
(d)
Transition
Depth (m)
0
−500
−1000
−1500
−2000
0
100
Angle (degrees)
φ1
φ2
ū
−ū

Figure 7.

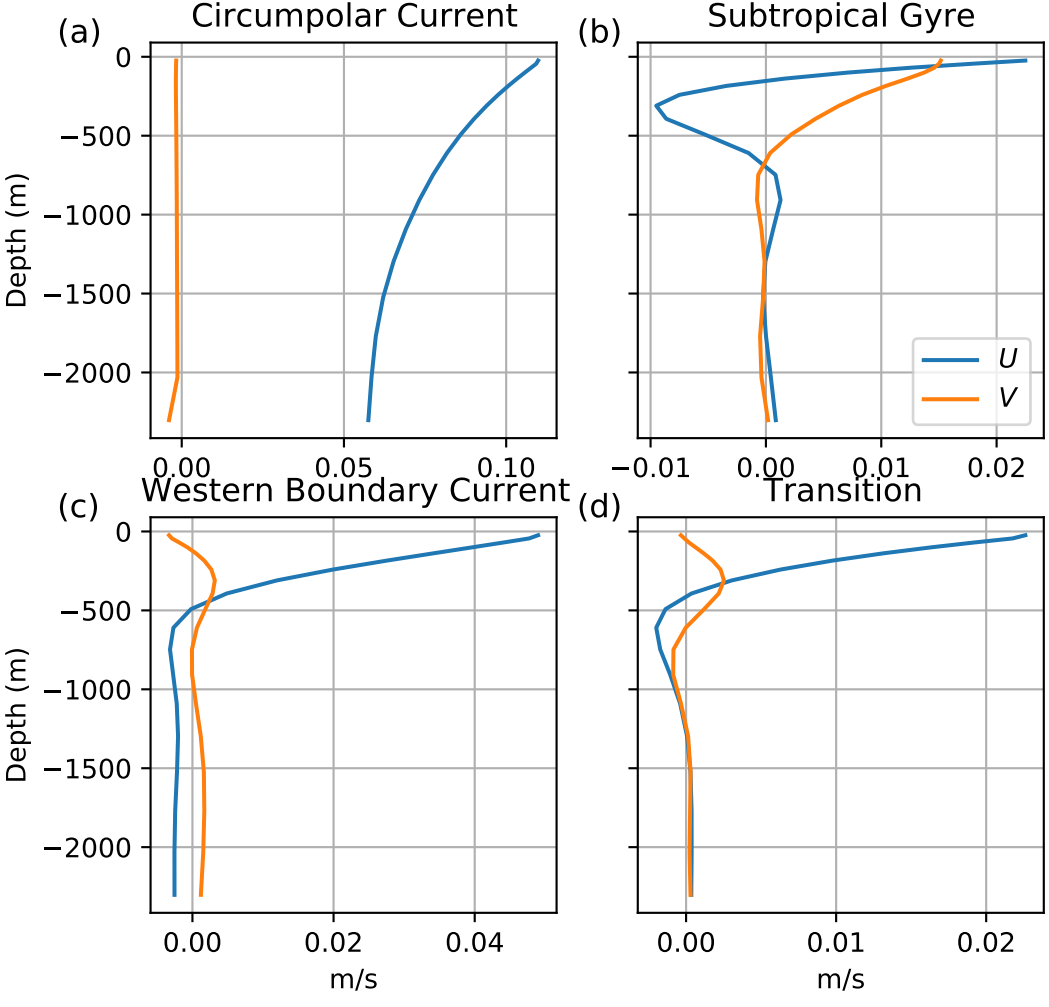
(a)
Circumpolar Current
(b)
Subtropical Gyre
(c)
Western Boundary Current
(d)
Transition
Depth (m)
0
−500
−1000
−1500
−2000
0.00
0.05
0.10
−0.01
0.00
0.01
0.02
0.04
m/s
U
V

Figure 8.

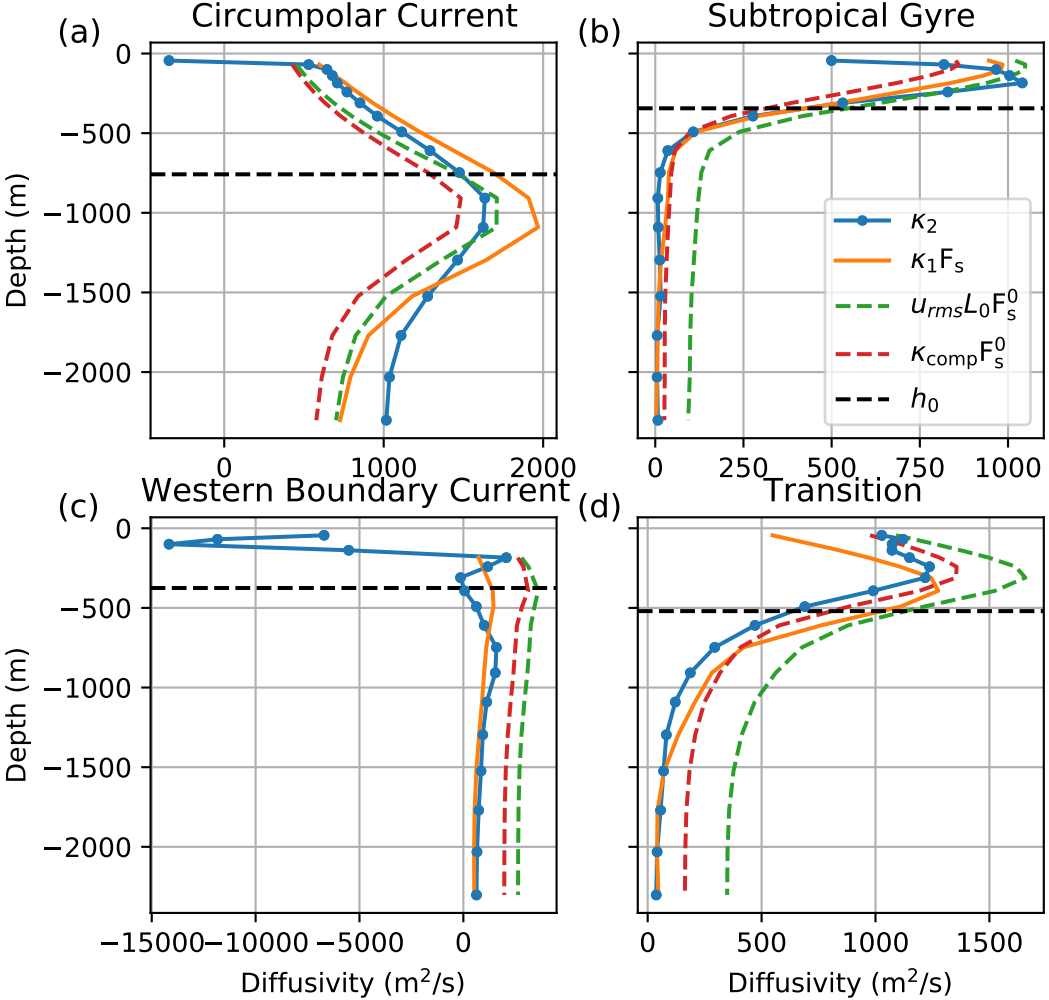
(a)
Circumpolar Current
(b)
Subtropical Gyre
(c)
Western Boundary Current
(d)
Transition
Depth (m)
Diffusivity (m^2/s)
κ_2
$\kappa_1 F_s$
$u_{rms} L_0 F_s^0$
$\kappa_{comp} F_s^0$
h_0

Figure 9.

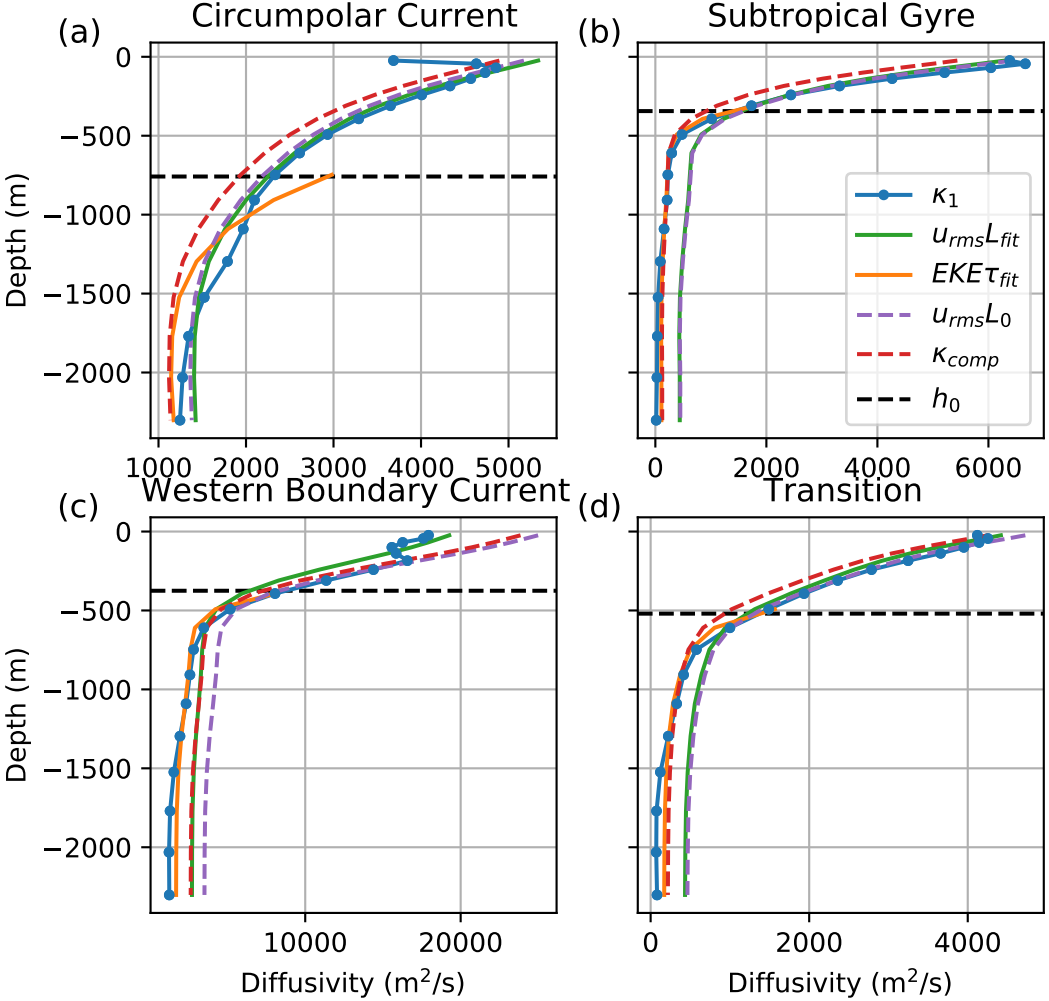
(a)
Circumpolar Current
(b)
Subtropical Gyre
(c)
Western Boundary Current
(d)
Transition
Depth (m)
Diffusivity (m^2/s)
κ_1
$u_{rms}L_{fit}$
$EKE\tau_{fit}$
$u_{rms}L_0$
κ_{comp}
h_0

Figure 10.

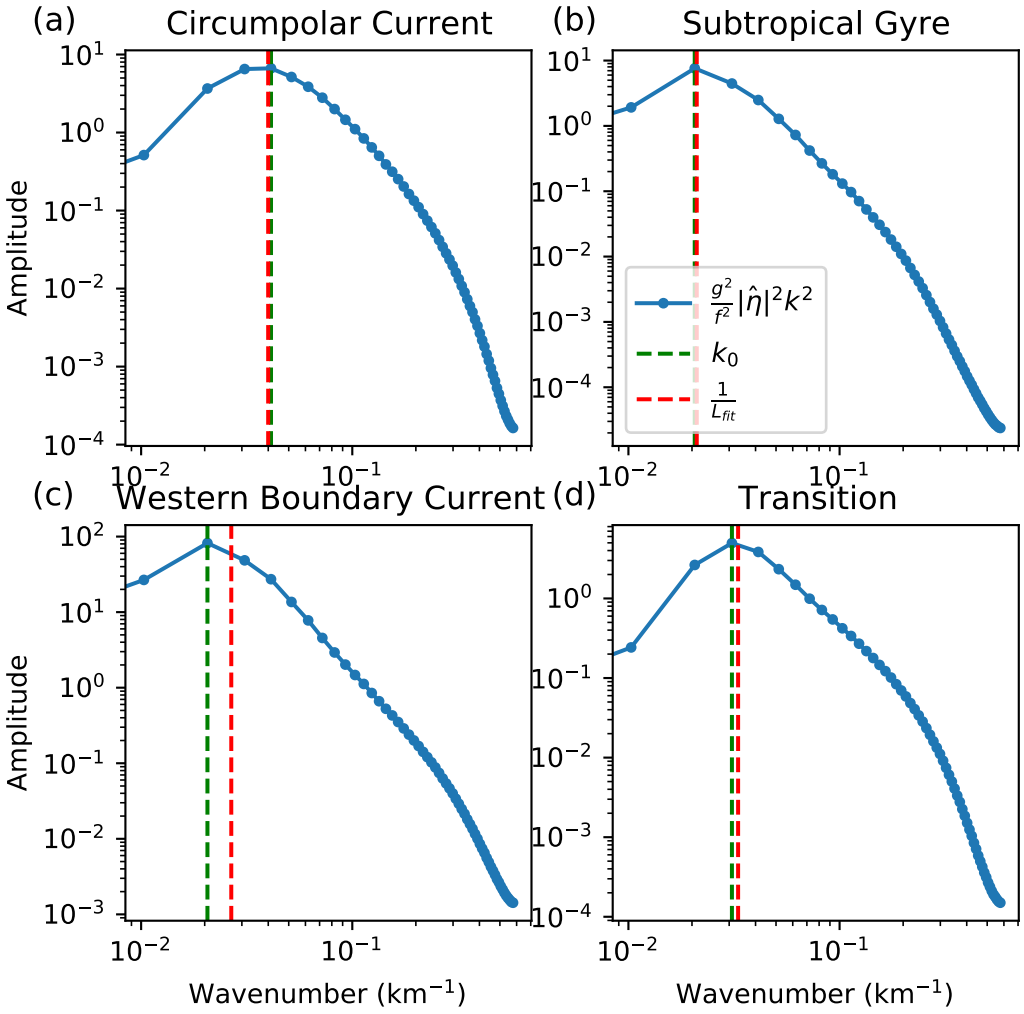
(a)
Circumpolar Current
(b)
Subtropical Gyre
(c)
Western Boundary Current
(d)
Transition
Amplitude
Wavenumber (km^{-1})
$\frac{g^2}{f^2}|\hat{\eta}|^2k^2$
k_0
$\frac{1}{L_{fit}}$

Figure 11.

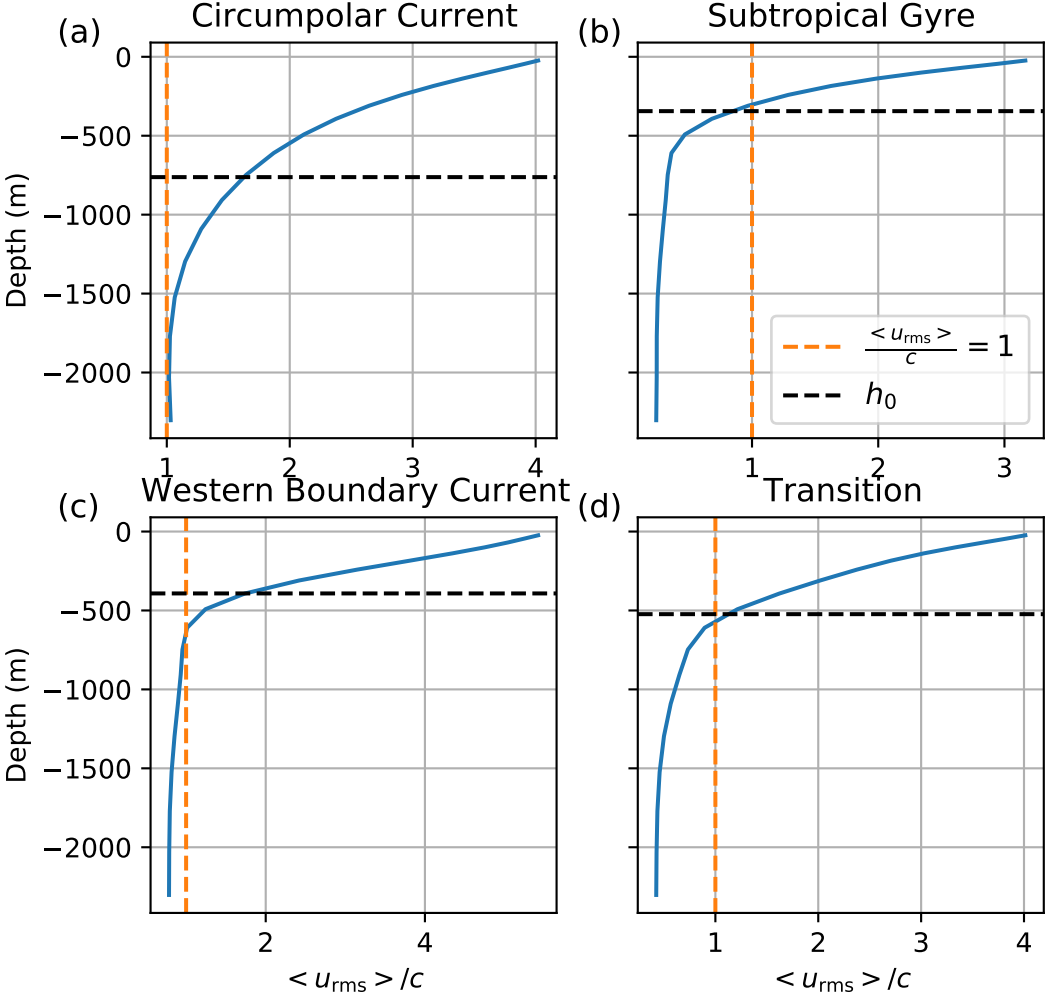
(a)
Circumpolar Current
(b)
Subtropical Gyre
(c)
Western Boundary Current
(d)
Transition
Depth (m)
0
−500
−1000
−1500
−2000
1
2
3
4
$\frac{< u_{\mathrm{rms}} >}{c} = 1$
h_0
$< u_{\mathrm{rms}} > /c$

Figure A1.

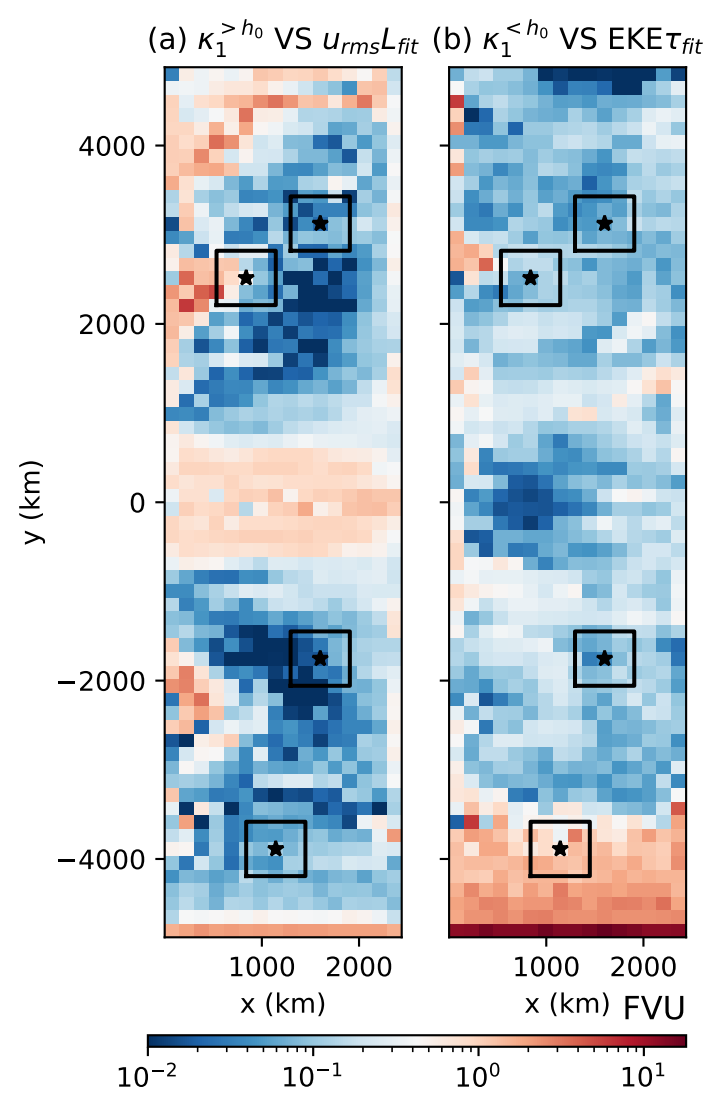
(a) $\kappa_1^{>h_0}$ VS $u_{rms}L_{fit}$
(b) $\kappa_1^{<h_0}$ VS EKEτ_{fit}
4000
2000
0
−2000
−4000
y (km)
1000
2000
x (km)
1000
2000
x (km)
FVU
10^{-2}
10^{-1}
10^{0}
10^{1}

Figure A2.

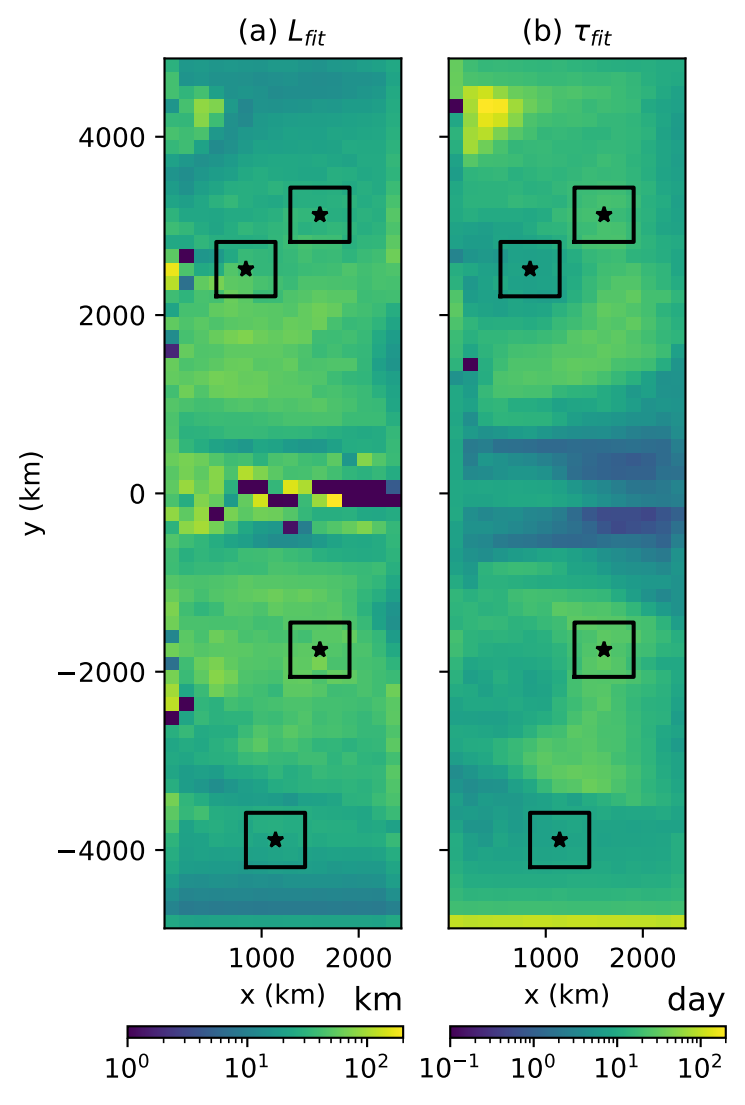
(a) L_{fit}
(b) τ_{fit}
4000
2000
0
−2000
−4000
y (km)
1000
2000
x (km)
km
day
10^0
10^1
10^2
10^{-1}

Figure A3.

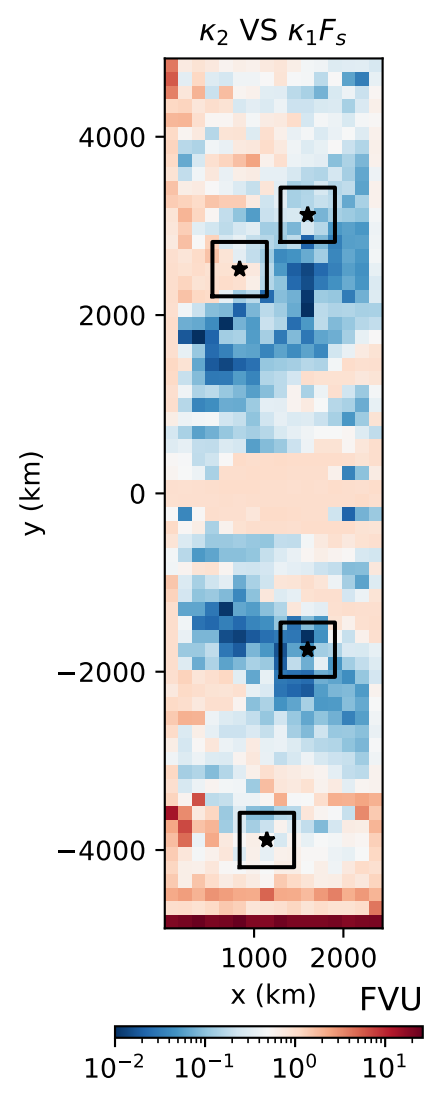
κ_2 VS $\kappa_1 F_s$
4000
2000
0
−2000
−4000
y (km)
1000
2000
x (km)
FVU
10^{-2}
10^{-1}
10^{0}
10^{1}